UNIVERSITY OF OKLAHOMA

GRADUATE COLLEGE

THE SEASONALITY OF MADDEN-JULIAN OSCILLATION (MJO) TELECONNECTIONS

A THESIS

SUBMITTED TO THE GRADUATE FACULTY

in partial fulfillment of the requirements for the

Degree of

MASTER OF SCIENCE

By

TATIANA ESTEVA-INGRAM
Norman, Oklahoma
2023

Downloaded from SHAREOK. Persistent Handle URL: https://hdl.handle.net/11244/337928

THE SEASONALITY OF MADDEN-JULIAN OSCILLATION (MJO) TELECONNECTIONS

A THESIS APPROVED FOR THE
SCHOOL OF METEOROLOGY

BY THE COMMITTEE CONSISTING OF

Dr. Naoko Sakaeda, Chair

Dr. Kathleen Pegion

Dr. Jason Furtado

© Copyright by TATIANA ESTEVA-INGRAM 2023
All Rights Reserved.

Dedication

I dedicate this work to my mother, my best friend, as without her none of this would be possible. She always encouraged me to be my true self, find my passions in this world, and help the people I can. I am eternally grateful for the opportunities you gave me, no matter the cost to you. I love you forever and this is for you.

Acknowledgements

I would like to share my appreciation for Dr. Naoko Sakaeda for taking me into her group, allowing me to grow as both a researcher and person. This process has been challenging but immensely rewarding with her as my advisor and I truly appreciate the time we have spent together. I also would like to acknowledge NSF and the grant (NSF 2303506) that funds the work I do. I want to thank my committee members for their time and effort into making this finished project. I extend my appreciation to all my friends, old and new, that gave me the space to be myself and supported me through this adventure. I give my love to my mom, dad, and the rest of my family for their endless support and love allowing me to get where I am today. I could go on forever, so know that if you were missed, I do acknowledge and thank you.

Table of Contents

Dedication **iv**

Acknowledgements **v**

List Of Tables **viii**

List Of Figures **ix**

Abstract **xiii**

1 Introduction **1**

2 The Seasonality of MJO Teleconections **8**
2.1 Data and Methods 8
2.2 Results 11
2.2.1 Determining our Patterns of Interest 12
2.2.2 Leading Mode One 13
2.2.3 Leading Mode Two 15
2.2.4 Leading Mode Three 17
2.3 Last Thoughts 18

3 Diagnosis of MJO Seasonal Teleconnections through the Rossby Wave Source (RWS) **27**
3.1 Definition of the RWS 28
3.2 Data and Methods 29
3.3 Results 30
3.3.1 Seasonal Differences in the MJO-Generated RWS 30
3.3.2 Seasonal Connections between MJO-Generated RWS and the Formation of Extratropical EOF Modes 32
3.3.2.1 First EOF Modes of the Seasons 32
3.3.2.2 Second EOF Modes of the Seasons 34
3.3.2.3 Third EOF Modes of the Seasons 37
3.3.3 Diagnosis of Contributing Processes to RWS 39
3.3.4 Relative Sensitivity of RWS to Seasonal MJO Anomalies and Background State 42
3.4 Summary 46

4 Conclusions **61**

Reference List **66**

List Of Tables

2.1 Number of seasonal sample days and the number of active MJO days from March 1979 to August 2018. 9

List Of Figures

1.1 Anomalous rainfall rate for each phase of the MJO. The green shading indicates above-average rainfall (enhanced convection) whereas the brown shading indicates below-average rainfall (suppressed convection). Taken from Gottschalck (2014). 6
1.2 Diagram of the different pathways that the MJO [cloud and purple shading] is able to influence/impact the extratropics via teleconnections, atmospheric rivers, or blocking. Taken from Stan et al. (2020). 7

2.1 Subplotted seasonal OMI composites of anomalous 200-mb (m) where the blue shading indicates anomalous lower heights and troughing while the red shading indicated anomalous higher heights and ridging. The figure includes phase 4 and 8 of the MJO where panels (a,b) are winter, (c,d) are spring, (e,f) are summer and (g,h) are fall respectively. The black stipple dots seen denote locations where p<0.1 when using a Monte Carlo test. 19
2.2 Seasonal correlation coefficients between MJO phase 200-mb height anomalies and various EOF modes (Regression of 200-mb height anomalies onto the standardized PC time series of daily mean North Pacific 200-mb anomalous heights (m)) Sub-panel (a) is winter, (b) is the spring, (c) is the summer, and (d) is the fall EOF. The black stipple dots seen denote locations where p<0.1 when using a Monte Carlo test. 20
2.3 Regression of 200-mb height anomalies onto the standardized PC1 time series of daily mean North Pacific 200-mb anomalous heights (m) where the blue shading indicated anomalous lower heights and troughing while the red shading indicates anomalous higher heights and ridging. Subpanel (a) is winter, (b) is the spring, (c) is the summer, and (d) is the fall EOF1 where the amount of variance explained for each seasonal EOF1 is indicated. 21
2.4 Seasonal anomalous probability of occurrence of each season's PC1 which was found doing the EOF analysis where panel (a) is winter, (b) is spring, (c) is summer, and (d) is fall. The color bar indicates anomalous frequency where purple shading indicates the pattern is more likely to occur compared to climatology and the orange shading indicates the pattern is less likely to occur compared to climatology. The black stipple dots seen denote points where p<0.1 when using a Monte Carlo test. 22

2.5 Regression of 200-mb height anomalies onto the standardized PC2 time series of daily mean North Pacific 200-mb anomalous heights (m) where the blue shading indicated anomalous lower heights and troughing while the red shading indicates anomalous higher heights and ridging. Subpanel (a) is winter, (b) is the spring, (c) is the summer, and (d) is the fall EOF1 where the amount of variance explained for each seasonal EOF2 is indicated. 23
2.6 Seasonal anomalous probability of occurrence of each season's PC2 which was found doing the EOF analysis where panel (a) is winter, (b) is spring, (c) is summer, and (d) is fall. The color bar indicates anomalous frequency where purple shading indicates the pattern is more likely to occur compared to climatology and the orange shading indicates the pattern is less likely to occur compared to climatology. The black stipple dots seen denote points where p<0.1 when using a Monte Carlo test. 24
2.7 Regression of 200-mb height anomalies onto the standardized PC3 time series of daily mean North Pacific 500-mb anomalous heights (m) where the blue shading indicated anomalous lower heights and troughing while the red shading indicates anomalous higher heights and ridging. Subpanel (a) is winter, (b) is the spring, (c) is the summer, and (d) is the fall EOF3 where the amount of variance explained for each seasonal EOF3 is indicated. 25
2.8 Seasonal anomalous probability of occurrence of each season's PC3 which was found doing the EOF analysis where panel (a) is winter, (b) is spring, (c) is summer, and (d) is fall. The color bar indicates anomalous frequency where purple shading indicates the pattern is more likely to occur compared to climatology and the orange shading indicates the pattern is less likely to occur compared to climatology. The black stipple dots seen denote points where p<0.1 when using a Monte Carlo test. 26

3.1 Subplotted seasonal OMI composites of anomalous 200-mb RWS generated from the MJO . The figure includes phase 4 and 8 of the MJO where panels (a,b) are winter, (c,d) are spring, (e,f) are summer and (g,h) are fall respectively. The black stipple dots seen denote locations where p<0.1 when using a Monte Carlo test. 47
3.2 Subplotted seasonal composite of climatological (1981-2010) absolute vorticity. The figure includes the anomalous divergent winds from phase 4 and 8 of the MJO where panels (a,e) are winter, (b,f) are spring, (c,g) are summer and (d,h) are fall respectively. 48
3.3 Subplotted seasonal composite of the MJO-generated RWS' for a positive PC1 index. Day-0 indicates the day when the PC1 > 1 and Day-10 Lag indicates 10 days before the PC1 > 1 is observed. Sub-panels (a,e) are winter, (b,f) are the spring, (c,g) are the summer, and (d,h) are the fall. 49

3.4 Subplotted seasonal composite of the MJO-generated RWS' for a negative PC1 index. Day-0 indicates the day when the PC1 < -1 and Day-10 Lag indicates 10 days before the PC1 < -1 is observed. Sub-panels (a,e) are winter, (b,f) are the spring, (c,g) are the summer, and (d,h) are the fall. 50
3.5 Subplottted seasonal regression coefficients between the OMI RWS' composites and the positive and negative PC1's RWS' for Day-0 and Day-5, -10, -15 lags. Sub-panels (a,e) are winter, (b,f) are the spring, (c,g) are the summer, and (d,h) are the fall. 51
3.6 Subplotted seasonal composite of the MJO-generated RWS' for a positive PC2 index. Day-0 indicates the day when the PC2 > 1 and Day-10 Lag indicates 10 days before the PC2 > 1 is observed. Sub-panels (a,e) are winter, (b,f) are the spring, (c,g) are the summer, and (d,h) are the fall. 52
3.7 Subplotted seasonal composite of the MJO-generated RWS' for a negative PC2 index. Day-0 indicates the day when the PC2 < -1 and Day-10 Lag indicates 10 days before the PC2 < -1 is observed. Sub-panels (a,e) are winter, (b,f) are the spring, (c,g) are the summer, and (d,h) are the fall. 53
3.8 Subplottted seasonal regression coefficients between the OMI RWS' composites and the positive and negative PC2's RWS' for Day-0 and Day-5, -10, -15 lags. Sub-panels (a,e) are winter, (b,f) are the spring, (c,g) are the summer, and (d,h) are the fall. 54
3.9 Subplotted seasonal composite of the MJO-generated RWS' for a positive PC3 index. Day-0 indicates the day when the PC3 > 1 and Day-10 Lag indicates 10 days before the PC3 > 1 is observed. Sub-panels (a,e) are winter, (b,f) are the spring, (c,g) are the summer, and (d,h) are the fall. 55
3.10 Subplotted seasonal composite of the MJO-generated RWS' for a negative PC3 index. Day-0 indicates the day when the PC3 < -1 and Day-10 Lag indicates 10 days before the PC3 < -1 is observed. Sub-panels (a,e) are winter, (b,f) are the spring, (c,g) are the summer, and (d,h) are the fall. 56
3.11 Subplottted seasonal regression coefficients between the OMI RWS' composites and the positive and negative PC3's RWS' for Day-0 and Day-5, -10, -15 lags. Sub-panels (a,e) are winter, (b,f) are the spring, (c,g) are the summer, and (d,h) are the fall. 57
3.12 Subplotted seasonal term contribution to the anomalous RWS using Eqn. 3.2 . Sub-panels are (a) winter, (b) spring, (c) summer, and (d) fall. Error bars are the bottom and top 5% of a Monte Carlo simulation of 1000 iterations. 58

3.13 Subplotted seasonal phase 4 composite of the observed RWS', the Annual MJO RWS' from Eqn. 3.3. and the Annual Background RWS' from Eqn. 3.4. Sub-panels are (a,b,c) are winter, (d,e,f) are spring, (g,h,i) are summer, and (j,k,l) are fall. 59
3.14 Subplotted seasonal phase 8 composite of the observed RWS', the Annual MJO RWS' from Eqn. 3.3. and the Annual Background RWS' from Eqn. 3.4. Sub-panels are (a,b,c) are winter, (d,e,f) are spring, (g,h,i) are summer, and (j,k,l) are fall. 59
3.15 Subplotted seasonal correlation coefficients between the observed RWS' with the Annual MJO RWS' and Annual Background RWS'. Correlation coefficients were calculated for the whole domain along with a subdomain (20-45 °N and 90-120 °E). Sub-panel (a) is winter, (b) is spring, (c) is summer, and (d) is fall. 60

Abstract

The Madden Julian Oscillation (MJO) is a tropical intraseasonal phenomenon that is known to generate teleconnections like the Pacific North American and the North Atlantic Oscillation patterns in boreal winter, but knowledge about MJO teleconnections is limited during other seasons. Therefore, to advance the prediction skill of the extratropics on the subseasonal-to-seasonal (S2S) using the MJO as a predictor, it is important to better understand the seasonal relationship between the MJO and its teleconnections.

To improve the S2S predictions during all seasons, this research demonstrates the strong seasonal variability of MJO teleconnections and investigates the causes of this seasonality using reanalysis and satellite data. We find that the MJO is tied to different leading modes of extratropical circulation that vary seasonally. While the MJO is strongly tied to some leading modes of the extratropics in winter, the MJO has weak relationships to the extratropical leading modes in other seasons, limiting the usability of the MJO as an S2S prediction tool. This seasonal variability in the strength and location of MJO teleconnection was found to be strongly related to the Rossby Wave Source (RWS) generated by the MJO. The generation of the RWS is determined by the seasonal location of the subtropical jet along with the strength and phase of the MJO. While the seasonal background state is often thought to play an important role, this work finds that the seasonal state of the MJO has a greater impact on determining the observed seasonal RWS patterns. This study offers an understanding that our current knowledge of MJO teleconnections during boreal winter would have limitations if applied to the other seasons and should be modified. Our current research indicates that the usability of the MJO as an S2S prediction tool in other seasons may depend on finding "windows of opportunities" that strengthen the ability of the MJO to form teleconnection patterns, such as other sources of interannual variability.

Chapter 1

Introduction

The Madden-Julian Oscillation (MJO) is a tropical convective phenomenon that has the ability to not only influence weather in the tropics but the extratropics as well. A way that the MJO has the capability to impact the extratropics is through teleconnections. Teleconnections are a linkage of weather events in distant regions. It is widely recognized that the MJO is at its strongest in boreal winter (Zhang and Dong 2004), so previous studies have mainly examined MJO teleconnections in boreal winter. However, studies on MJO teleconnections in the other seasons are limited, which inhibits our application of the MJO as a source of predictability in other seasons. This work aims to better understand MJO teleconnections in other seasons.

The unique planetary, intraseasonal behavior and structure of the MJO leads to its pronounced influence on extratropics. The MJO (Madden and Julian 1971, 1972) is defined as a tropical atmosphere-ocean system of planetary-scale convective anomalies that propagates eastward at a speed of about 5 m/s. The MJO has a life cycle of about 30-60 days, where the enhanced convection of the MJO will initiate over the Indian Ocean, and move eastward until the enhanced convection begins to dissipate over the central to eastern Pacific Ocean (Fig. 1.1). By convention, the MJO is broken down into eight phases in order to track the location of the suppressed/enhanced convection. The positive rainfall anomalies (green shading) in Fig.1.1 indicate the enhanced convection of the MJO that travels eastward over the Indian Ocean and begins to decay over the Eastern Pacific in the later phases. Figure 1.1 also highlights that the region

of enhanced convection is accompanied by a region of suppressed convection either to its east or west, and they both propagate eastward. The circulation structure of the MJO at the lower troposphere consists of two cyclonic Rossby Waves, north and south of the equator, at the west of the enhanced convection, and similar but anticyclonic Rossby waves appear at the west of the suppressed convection (at 850hPa; Kiladis et al. 2005). On the east side of the convection, a Kelvin wave response is seen (Kiladis et al. 2005). These Rossby and Kelvin wave circulations are associated with the lower-tropospheric convergence around the convection and rising air, supporting the enhancement of the convection while the opposite is true for the area of suppressed convection. The circulation responses that are associated with the Rossby wave or the upper-level divergence allow the MJO to perturb midlatitude flow and generate extratropical teleconnections.

As the circulation response to MJO convection can expand into the subtropics to interfere with the subtropical jet, the MJO can have impacts on the extratropical latitudes, including tropical cyclone tracks, polar sea ice, and the ability to generate MJO teleconnections (Jiang et al. 2020). We can see some effects of the MJO on tropical-extratropical interactions with Fig. 1.2. The MJO, the purple shading/cloud symbol, can impact a variety of midlatitude weather phenomena globally. Specifically, the dashed arrows in Fig. 1.2 indicate that the MJO can influence Eurasia, North Pacific, and Atlantic through teleconnections. The Pacific North American (PNA) and North Atlantic Oscillation patterns are examples of extratropical modes that can be provoked by the MJO on the intraseasonal time scale impacting weather in North America (MORI and WATANABE 2008; Cassou 2008).

The connection between the MJO and PNA is particularly seen in boreal winter, which has been studied extensively to understand how the MJO generates teleconnection through the generation of midlatitude Rossby waves. The PNA pattern is defined

as a trough in east/central North Pacific, a ridge over Rocky Mountains, and a trough over eastern North America (Leathers et al. 1991). Due to such circulation patterns, the PNA has a considerable influence on temperature along with precipitation in the United States. Zhang and Dong (2004) showed that waves that move into the PNA region originate from a Rossby Wave Source (RWS). The MJO can generate a RWS by its anomalous upper-level divergent flow that interacts with the strong absolute vorticity gradient along the midlatitude North Pacific westerly jet (Seo and Lee 2017; Wang et al. 2020). The Rossby wave forced by tropical forcing can then propagate downstream to form the PNA (more details in Seo and Lee 2017). The most effective way to create a PNA-like pattern is to create an RWS at the exit of the Asian-Pacific jet. MORI and WATANABE (2008) show that there is a clear phase locking between the MJO and PNA. During active convection tied to the MJO over the Bay of Bengal, the probability that a negative phase of the PNA develops is at its highest while the opposite is true for inactive convection and a positive PNA.

While the aforementioned previous studies only examined the MJO teleconnections and their dynamics in boreal winter, the usability of the MJO as a S2S predictor has been suggested in other seasons. For example, there were significant increases in springtime US tornado and hail frequency found 3 to 4 weeks after the associated strongest upper-level divergence from the MJO events that make it pass the Maritime Continent (Miller et al. 2022). In the boreal summer, the MJO is associated with the occurrence of California heat waves and tropical cyclone frequency (Lee and Grotjahn 2019; Belanger et al. 2010). The most reliable tropical cyclone forecasts in the Atlantic initially had a convectively active MJO over the Indian Ocean due to favorable conditions (generated from the MJO) for the first two weeks in model prediction (Belanger et al. 2010). However, the underlying dynamics relating the MJO to these seasonal

extreme weather events are not fully understood. Furthermore, with a warming climate, it is possible that weather extremes could occur more frequently which can have devastating consequences. In order to mitigate these consequences, the ability to have accurate forecasts on the S2S timescale becomes imperative.

Given the seasonally-dependent impact of the MJO on global weather phenomena, a greater understanding of the MJO teleconnections and its seasonality is important to advance S2S prediction skill. We discussed the PNA as a MJO teleconnection pattern that is known to be strongest in winter, but MJO teleconnections in other seasons are less studied. Do these seasonal teleconnection patterns require a trigger from the MJO or a dynamical process that differs from boreal winter? The MJO is viewed as a source of predictability on the subseasonal-to-seasonal (S2S) timescale and to use the MJO as a S2S predictor in other seasons, an understanding of the seasonal changes of the MJO teleconnections is required. There are two main sources of variability that can lead to the seasonality of MJO teleconnections, which are the seasonal cycles of the MJO itself and the extratropics.

Many studies have confirmed that the MJO and its characteristics like propagation, amplitude, and structure vary seasonally (Adames et al. 2016; Zhang and Dong 2004), which can lead to the seasonality of MJO teleconnection as well. MJO signal strength is strongest in the boreal winter and weakest in the boreal summer, but the location of the strongest signal does not appear exactly on the equator. It has been shown that the signal of the MJO drifts meridionally where it peaks south of the equator in the boreal winter and north of the equator in the boreal summer months (Zhang and Dong 2004). These seasonal changes in the location and amplitude of the MJO are thought to be modulated by the seasonal changes in the background near-surface winds and associated areas of moisture convergence (Adames et al. 2016; Zhang and Dong 2004). In response to the seasonality of the MJO, the amplitude of the Rossby

Waves associated the MJO will also be strongest in the winter hemisphere (Adames et al. 2016). The strength and meridional extent of these Rossby Waves can influence how the MJO modulates extratropical latitudes.

In addition to the seasonality of the MJO, there is also a strong seasonality in the extratropical circulation that would influence the seasonality of MJO teleconnections. The flow of the subtropical jet is crucial in determining the propagation features of the Rossby waves generated from the MJO (Henderson et al. 2017). It has been shown in previous studies that the subtropical jet has seasonal variability in its' location and strength (Maher et al. 2020). Variability in the jet will cause seasonal changes in the extratropical circulation patterns. Furthermore, the interactions between the MJO and subtropical jet will vary seasonally as well impacting MJO teleconnection generation.

The aforementioned seasonality of the MJO and extratropics is expected to generate seasonality in MJO teleconnections. Given the gap of knowledge on how these two factors generate seasonality of MJO teleconnections, there is a strong need to improve our understanding of it. Filling this knowledge gap is important as the MJO is considered an important source of S2S predictability. With over 100 billion dollars of damages due to weather events (Vitart and Robertson 2018), there is a demand to find ways to mitigate these socio-impacts via increased S2S prediction skill. As a potential source of predictability on the S2S timescale due to its intraseaonsal behavior, the MJO can provide longer lead time to weather events benefiting society. By better understanding the seasonality of these teleconnections, we can better understand their impacts and learn how we can use the MJO as an S2S predictor in different seasons.

Given the knowledge gap of the MJO teleconnections outside of boreal winter, the main goal of the following work is to understand the seasonality of MJO teleconnections. Using reanalysis and satellite data, this paper aims to understand and answer the following two questions:

1. Do MJO teleconnections vary seasonally?

2. Why do the MJO teleconnections vary seasonally?

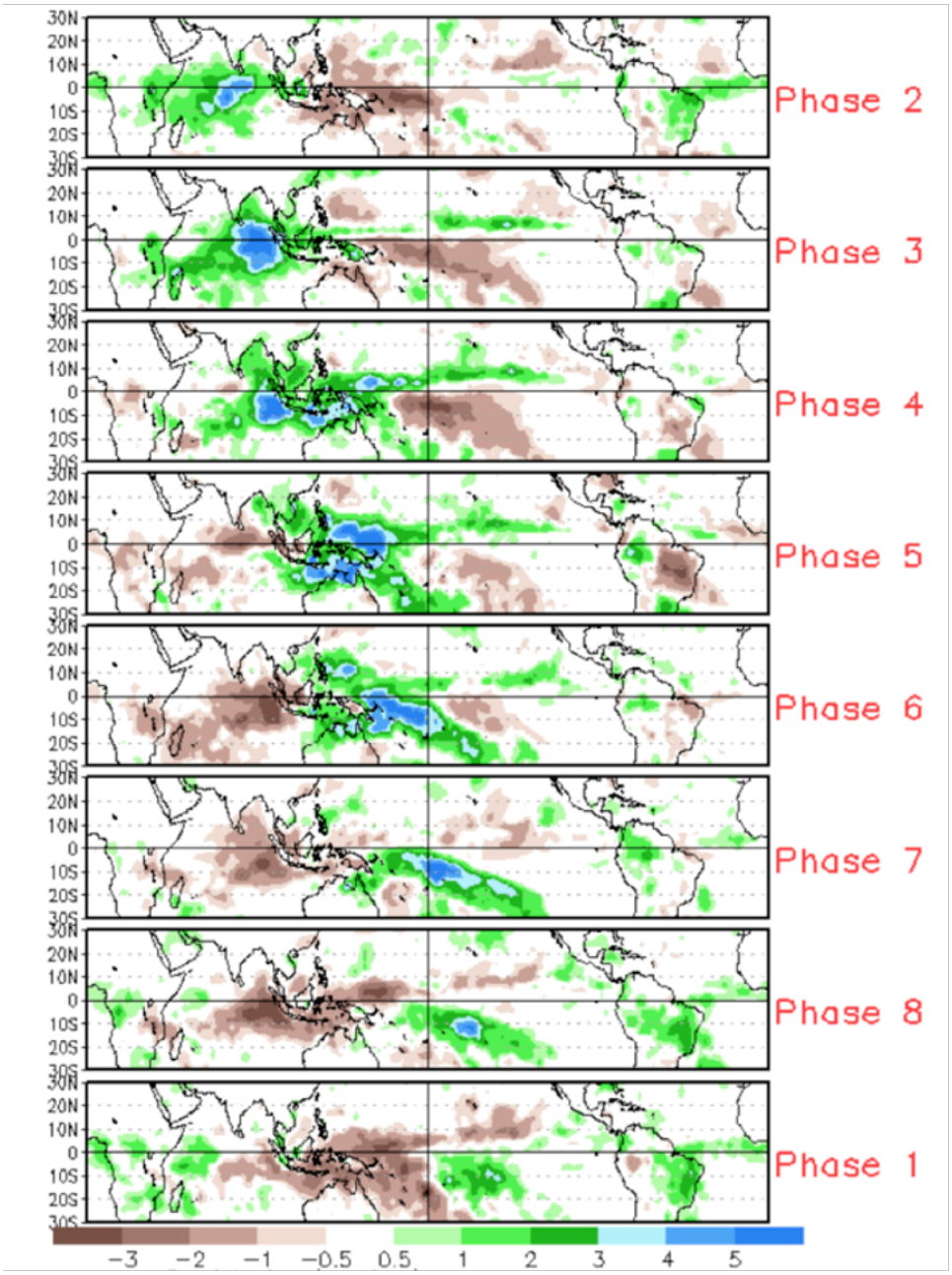

Figure 1.1: Anomalous rainfall rate for each phase of the MJO. The green shading indicates above-average rainfall (enhanced convection) whereas the brown shading indicates below-average rainfall (suppressed convection). Taken from Gottschalck (2014).

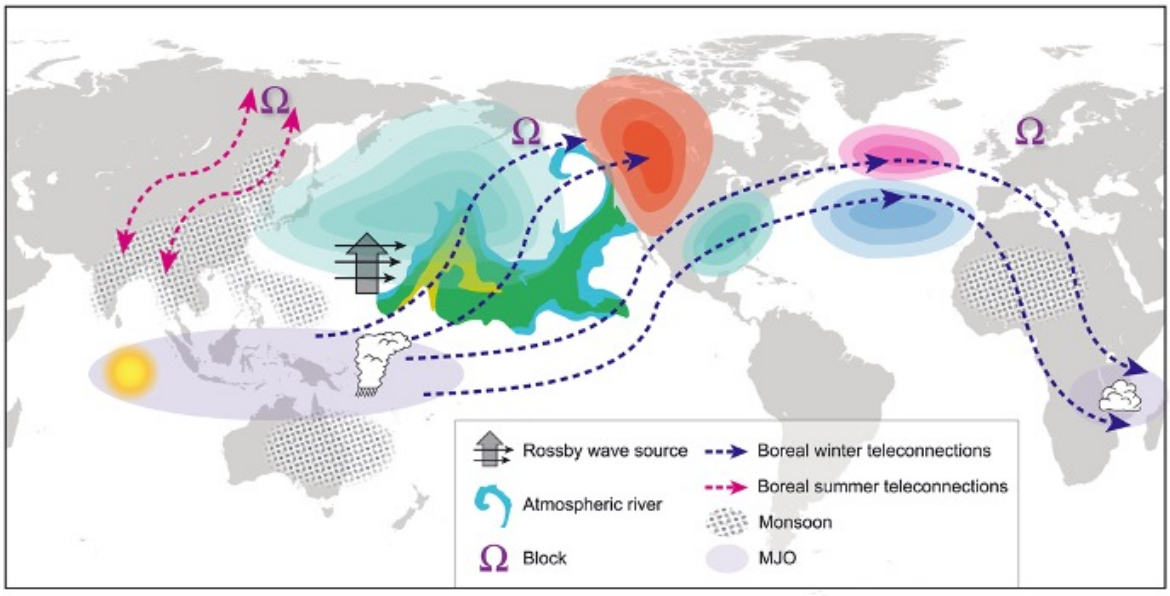

Figure 1.2: Diagram of the different pathways that the MJO [cloud and purple shading] is able to influence/impact the extratropics via teleconnections, atmospheric rivers, or blocking. Taken from Stan et al. (2020).

Chapter 2

The Seasonality of MJO Teleconections

The objective of this chapter is to understand whether there is observed seasonality in the MJO teleconnections. This will be achieved by compositing height patterns with respect to MJO phases, finding the seasonally dominant teleconnection pattern, and the probability of these dominant patterns occurring with respect to MJO phase. These analyses will demonstrate the strong seasonality of MJO teleconnections and the occurrence of which extratropical modes are associated with the MJO in each season.

2.1 Data and Methods

In order to track the location and strength of the MJO, the OLR MJO Index (OMI; Kiladis et al. 2014) was used. The OMI is calculated by doing an Empirical Orthogonal Function (EOF) analysis of spatially-gridded OLR (Kiladis et al. 2014) and provided the daily phase and amplitude of the MJO. It is also known to capture seasonal variations of the MJO more accurately than other indices like the Real-time Multivariate (RMM; Wheeler and Hendon 2004). This section also uses reanalysis 200-mb heights data from the ECMWF-ERA5 database (Hersbach et al. 2020). Analysis for this chapter and Chapter 3 was done for each season which is defined as the following: Winter (December, January, February; DJF), Spring (March, April, May; MAM), Summer (June, July, August; JJA), and Fall (September, October, November; SON).

We determined the phase of the MJO each day from March 1979 to August 2018. To match the phase evolution of the RMM (Wheeler and Hendon 2004), we had to switch the sign of OMI's Principle Component (PC) 1 and the order of PC1 and PC2 per the instructions of the NOAA PSL website. After that, we found the arc-tangent of PC1 and PC2 to find the phase angle for each day and use the phase angle to determine the convectional 8 phases of the MJO, as done for the RMM. Then, to identify an active MJO, we found the sample standard deviation amplitude for each month. A typical method used to identify days of active MJO is by finding days with an OMI amplitude greater than one. However, due to strong differences in the MJO in each season/month, we calculate the monthly amplitude standard deviation to have an active definition that is more tailored to the seasonality of the MJO strength. If any day in that month had an OMI amplitude that is greater than the sample standard deviation, it was defined as a MJO active day and assigned its respective MJO phase number. If not, the day is considered inactive. Table 2.1 summarizes the number of identified MJO active days using our definition in each season, showing that our method identifies a similar number of MJO active days seasonally.

Season	**Sample Days**	**Active MJO Days**
Winter (DJF)	3,520	2,741
Spring (MAM)	3,680	2,969
Summer (JJA)	3,680	3,191
Fall (SON)	3,549	2,920

Table 2.1: Number of seasonal sample days and the number of active MJO days from March 1979 to August 2018.

By compositing anomalous 200-mb heights by MJO phases for each season, we evaluate the teleconnection pattern associated with the MJO. As previously mentioned, a

common teleconnection pattern found to be strongly associated with the MJO over the North Pacific is the PNA pattern in winter (MORI and WATANABE 2008; Seo and Lee 2017). MORI and WATANABE (2008) notated that a positive PNA is indicated by an anomalous trough over the North Pacific and an anomalous ridge when it is a negative PNA. To deepen the understanding of the seasonality of MJO teleconnections, we wanted to understand if the MJO had the ability to modulate the seasonally dominant extratropical patterns. We used EOF analysis on the anomalous 200-mb heights over the North Pacific, to extract the dominant extratropical patterns in each season. While the PNA is a dominant teleconnection pattern in boreal winter that the MJO is associated with (MORI and WATANABE 2008), the goal of this work is not to look only for the PNA pattern but the seasonality of any exhibited teleconnection pattern. To then understand how the MJO influences the leading modes of the extratropics, we then examined the probability distribution of their corresponding principal components (PCs) seasonally, during each phase of the MJO.

Monte Carlo simulations, with 1000 iterations, were performed on the height composites along with the anomalous probability distribution to test their statistical significance at the 90% confidence level. Monte Carlo simulations are re-sampling of data to test if any of the results were obtained by random chance. The re-sampling is done from a random set of dates within the same season, which is compared to the actual composite value to obtain its percentile of the score (p-value). If the p-value is less than 0.1, it is deemed significant and concluded that it did not happen by chance.

Finally, our analysis will be confined to the Northern Pacific Basin. Due to prior knowledge of a relationship between the North Pacific Basin and the MJO, like the MJO-induced PNA pattern (MORI and WATANABE 2008; Seo and Lee 2017), we will examine how the teleconnection of this basin varies seasonally. We also will mainly

present only phases 4 and 8 of the MJO to highlight teleconnections associated with similar but opposite-sign patterns of tropical precipitation.

2.2 Results

We first evaluated how the anomalous 200-mb height patterns change seasonally within the MJO phase. Figure 2.1 shows that the strongest amplitude of height anomalies is found in winter while the amplitude decreases in other seasons, and it is at its weakest in summer. Only in winter, we see a clear PNA-like pattern during MJO phase 4. Even for this same MJO phase, the height composites are not identical among the seasons, as seen from different strengths and locations of the anomalous troughs and ridges. For example, compared to winter, the eastern portion of the trough over western North America in spring retracts poleward and moves westward with the western portion of the trough extending slightly equatorward. In summer, the trough over the North Pacific is practically nonexistent but moves over the western United States. In fall, we can see a strong trough that extends from the (Arctic) pole. We can also see differences in the height composites of MJO phase 8 and while not shown, seasonal variability in the height composites is exhibited in the other phases of the MJO as well. Two points that can be drawn from this analysis are that, first, the height anomaly patterns associated with the MJO have a strong seasonal dependency. Second, the generation of a PNA-like pattern associated with the MJO is exclusively found in winter which is consistent with previous work (MORI and WATANABE 2008; Seo and Lee 2017).

2.2.1 Determining our Patterns of Interest

We demonstrated that MJO teleconnection in height patterns varies substantially with seasons. This seasonality of MJO teleconnection may be partly due to the fact that there are seasonally different dominant height mode/patterns in the extratropics. The MJO may induce different seasonal teleconnection by bringing out seasonally different dominant patterns due to the intrinsic atmospheric dynamics of the extratropics. Understanding which leading modes the MJO modulates seasonally is also relevant to the application of the MJO as an S2S predictor. If the MJO influences the most dominant pattern, EOF1, in one season but higher order EOF patterns in other seasons, it indicates that the MJO may have a greater source of predictability in seasons when it more strongly influences the most dominant pattern.

To first evaluate which EOF-mode(s) resembles the MJO-generated teleconnections patterns, we calculated the spatial correlations between each EOF pattern and anomalous 200-mb height composites of the MJO phases in each season. The spatial correlation was done after the anomalies were weighted by the latitude/area. This was then repeated up to the first 10 leading EOFs which explains, seasonally, at least 64.31% of the total variance. The resulting spatial correlations are shown in Fig. 2.2. Monte Carlo significance testing was done by randomly re-sampling of days in the season and re-calculating the height composites. Then, a spatial correlation between an EOF pattern with those re-sampled phase days was done, and p-values at a 90% confidence level were found.

Figure 2.2a shows that winter has multiple points of significance for the first two EOF patterns, indicating that MJO height composites strongly resemble the first two EOF patterns. However, except for EOF1 in the summer, the MJO teleconnection patterns in other seasons do not strongly resemble any particular EOF mode seen with the lack of significant points for more than 4 phases of the MJO. This ties back to the

seasonal usability of the MJO as an S2S predictor. In winter, the MJO could be a good source of S2S predictability because it strongly modulates the first two leading modes. In other seasons, however, the MJO may not be as useful in predicting an occurrence of a particular EOF mode. Spring (Fig. 2.2c) has one phase of significance for the first three EOF modes whereas summer (Fig. 2.2e) has multiple phases of significance for EOF1 and EOF3. Finally, fall has phases of significance for EOF 2 and EOF 3. This implies that the MJO would only weakly modulate the occurrences of these EOF modes with a specific phase.

Our goal is to understand why the MJO does or does not influence the dominant modes seasonally. Understanding how the MJO influences the most dominant modes, it can have implications for S2S prediction skill. Hence, we will focus on further understanding how the MJO influences the three most dominant modes, EOF1-3. We highlight these 3 modes and emphasize the seasonal difference in how the MJO is related to them in the following subsections.

2.2.2 Leading Mode One

Figure 2.3 shows the first leading mode, EOF 1, which has patterns that are distinct between seasons. There are differences in both the strength and positioning of the troughs/ridges. We see that winter (Fig.2.3a) has the strongest magnitude of EOF pattern with a trough that extends over the northern Pacific into the poles, a ridge over North America, with a weak ridge over the south Pacific and a weak trough over southern North America. We can also see that fall has a similar pattern to winter with differences in the positioning/extension and magnitude. Summer is weakest in magnitude and has a trough over the North central Pacific and a ridge that extends from the Northern subtropical Pacific into the northwestern Canada. However, spring has a similar pattern to winter with an opposite sign where spring's trough over the Atlantic

is connected to the poles whereas in winter, the trough in the Pacific is connected to the Poles.

To further understand how the MJO relates to the occurrence of EOF1 pattern, Fig. 2.4 shows the anomalous probability distribution of each season's PC1 in each MJO phase. It shows that phase 4 of the MJO does not present the same sign of the EOF1 pattern across the seasons. The positive probability anomalies (purple shading) at a chosen MJO phase indicates that the corresponding value of the PC1 is most likely to occur with that MJO phase whereas the negative anomalies (orange shading) indicate the opposite and lower probability of occurrence. Winter phase 4 is associated with an increased occurrence of the positive EOF1 pattern, indicated by the negative probability anomalies of negative PC1 and positive probability anomalies of positive PC1. In contrast, in summer, phase 4 produces the negative EOF1 pattern whereas phase 4 in fall seems to produce a higher chance of both strongly negative and positive EOF1. Spring does not seem to produce any EOF1 pattern during phase 4. We can verify these findings by comparing our EOF1 pattern (Fig. 2.3) and the OMI height composites (Fig. 2.1). In winter, we see in phase 4 height composite, there is a ridge over the central to eastern North America which is a similar location to the ridge in the EOF1 pattern but not as wide and is more southward. For spring, we can see that Fig. 2.1c and Fig. 2.3b do not have any similarity due to the height composite having a tripole of troughs and a ridge over the Pacific Basin in comparison to the EOF1 having a strong, latitudinal stretched ridge over the north Pacific with a weak trough underneath. We can see that there are seasonal differences in how phase 4 of the MJO interacts with its' EOF1 pattern.

At OMI phase 8, the opposite pattern to OMI phase 4 does not occur in all seasons. In winter, there is no prominent occurrence of the positive EOF1 during phase 8, whereas in the summer, phase 8 displays the positive EOF1 pattern. The two seasons,

spring and fall, that did not produce an EOF1 pattern in phase 4, produce a negative EOF1 pattern during phase 8. The previous statements can be verified with the similarities or lack of in the positioning of the troughs and ridges when comparing the seasonal OMI phase 8 height composite (Fig. 2.1b,d,f,h) to its respective EOF1 pattern (Fig. 2.3). Seasonally different modulation of the seasonal EOF1 by the MJO implies that knowledge about one season is not applicable to another. Figure 2.4 brings up the question of why there is still a significant influence of the MJO on the frequency distribution during certain phases but there is no significant correlation with EOF1 in all seasons. Since a composite is an average of all selected times, it could be that the composites are not revealing how the MJO modulates the occurrence of the EOF mode.

It is slightly unexpected that MJO phases 4 and 8 did not always produce the opposite EOF1 pattern, given that the tropical precipitation patterns are generally the same but opposite in sign. This expands the earlier point that teleconnection development induced by the MJO might need more certain/specific conditions to form other than the switch in the locations of MJO enhanced and suppressed convection. Further investigation will be done to understand why this is the case in the next chapter. Again, we highlight that winter knowledge of the relationship between the MJO and its teleconnections would not be fully applicable in other seasons and full usability of the MJO as a S2S predictor depends on understanding the seasonal differences of the MJO teleconnections.

2.2.3 Leading Mode Two

As indicated in section 2.2.1, the winter MJO has the strongest relationship with EOF2 and can be explained by the PNA-like structure of EOF2. Figure 2.5a,d show that the patterns of EOF2 in winter and fall are similar with only very slight positioning

and magnitude differences. The winter EOF2 pattern appears to show a PNA-like pattern as it has a consistent structure illustrated with Wallace and Gutzler (1981). Spring has a band of trough between 30-55 °N and ridge about 55-90 °N whereas summer as a 4 centers of alternating troughing and riding. With such distinct modes, knowledge about how the MJO could modulate one season's EOF2 mode would mean different things.

Figure 2.6, the anomalous probability distributions of PC 2, emphasizes the strong relationship between EOF2 and winter MJO. In winter, phase 4 frequently exhibits the positive EOF 2 pattern whereas phase 8 exhibits the negative. The similarities between the positive EOF2 pattern and OMI phase 4 height composite (Fig. 2.5 and Fig. 2.1a) in the location of troughs and ridges are displayed with slight positioning differences between the two. OMI phase 8 and the negative EOF2 pattern exhibited similarities as well. We note that the magnitudes of anomalous probabilities for winter are much greater than in Fig 2.4 alluding that the MJO might be tied closer to this second EOF pattern. This is consistent with Fig. 2.2a which had its most significant points/phases in the EOF2 mode. Since this EOF2 pattern more closely resembles the PNA pattern than EOF1, this could be the reason the MJO more strongly modulates EOF2. This would be in agreement with prior studies like (MORI and WATANABE 2008), as they indicated the highest chance of development of a negative PNA would occur around phases 3 and 4 and a positive PNA would occur around phases 7 and 8 of the MJO. Given the quadrature relationship of EOF1 and EOF2, they might be related where the EOF1 pattern often occurs before an MJO-induced PNA pattern (EOF2) is set up. This potential propagation relationship with PC1 and PC2 can be seen in the shifting pattern, where the positive correlations occur in later/subsequent phases of MJO from PC1 to PC2, in Fig. 2.2.

The weak relationships in the other seasons between the MJO and EOF2 can be explained by the lack of similarities between the seasonal EOF2 pattern and MJO height composites. Figure 2.6 demonstrates that OMI phases 4 and 8 in the seasons, except for winter, do not produce the opposite EOF2 pattern. Comparison between the two phase's height composites in each season to its' EOF2 pattern demonstrates the strong lack of similarities with orientation and presence of troughs and ridges. Furthermore, the amplitudes of anomalous frequency are not as strong as in winter alluding to the fact that the MJO in other seasons does not modulate its EOF2 which is consistent with Fig. 2.2.

2.2.4 Leading Mode Three

EOF3 seems to be more correlated with the spring MJO. The seasonal EOF3 has a similar location and orientation of the height anomalies except for summer (Fig. 2.7). There are centers of alternating ridges and troughs along with similar magnitudes. However, there are seasonal differences in the orientation of these troughs/ridges and whether these areas extend from the poles.

While the spring MJO has not been strongly tied with EOF1 and 2, it seems to be tied with the EOF3 pattern due to some similarities between the EOF3 pattern and height composites. The modulation of the EOF3 by the spring MJO can be visualized with Fig. 2.8b where Phase 4 and 8 of the MJO, in spring, produce the negative and positive EOF3 pattern, respectively. With relatively stronger amplitudes in anomalous frequency, this would imply a stronger relationship between the MJO and EOF3 in spring. By comparing Fig. 2.1c and Fig. 2.7b), the spring EOF3 pattern has a trough that extends from the southern Asian continent into the North Pacific and over most of North America where the OMI phase 4 height composite has ridges over the same general areas. The same comparison can be done in spring for OMI phase 8 and the

EOF3 pattern. The ability of the spring MJO to modulate the EOF3 pattern comes with the similarities between the MJO height composites and EOF3.

2.3 Last Thoughts

In summary of this chapter, we found that the MJO teleconnections patterns exhibit strong seasonality and we exclusively only see a PNA-like pattern to be associated with the MJO in winter. The patterns of each individual EOF mode are also distinct seasonally from each other. Furthermore, we found that the phases of the MJO do not produce troughs/ridges over the same area in each season. It was also established that the MJO is not tied to the first leading mode seasonally. With this, we emphasize that the previous knowledge about the MJO teleconnections in boreal winter (seen in studies like MORI and WATANABE 2008; Seo and Lee 2017) would have limitations if applied to other seasons. It also accentuates the need to have a better understanding of the factors causing the MJO teleconnection seasonality and differences in the exhibited signage of the EOF mode during MJO phase. With the understanding that the MJO only weakly modulates the dominant modes in other seasons, it would imply that the usability of the MJO as an S2S predictor would be limited in those seasons. Investigation into what is causing the seasonality of the MJO teleconnections is done in Chapter 3.

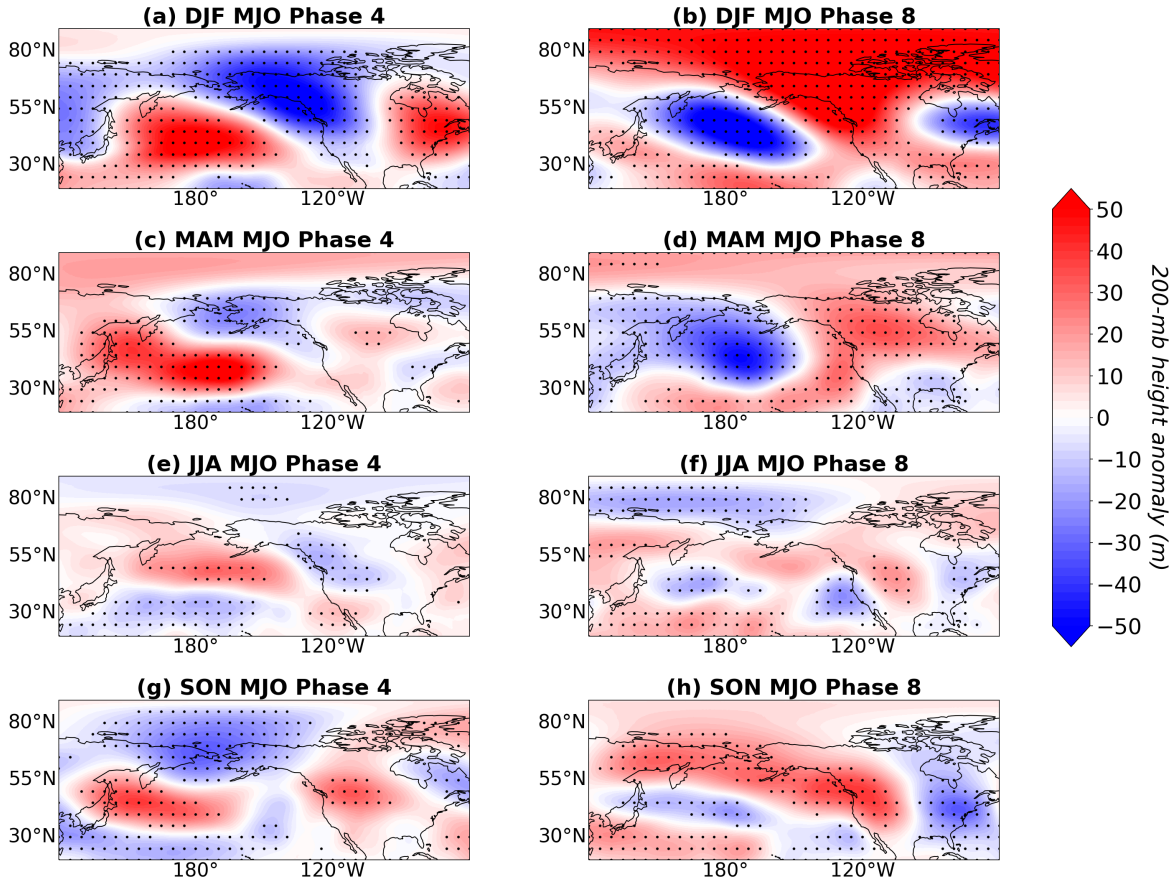

Figure 2.1: Subplotted seasonal OMI composites of anomalous 200-mb (m) where the blue shading indicates anomalous lower heights and troughing while the red shading indicated anomalous higher heights and ridging. The figure includes phase 4 and 8 of the MJO where panels (a,b) are winter, (c,d) are spring, (e,f) are summer and (g,h) are fall respectively. The black stipple dots seen denote locations where $p<0.1$ when using a Monte Carlo test.

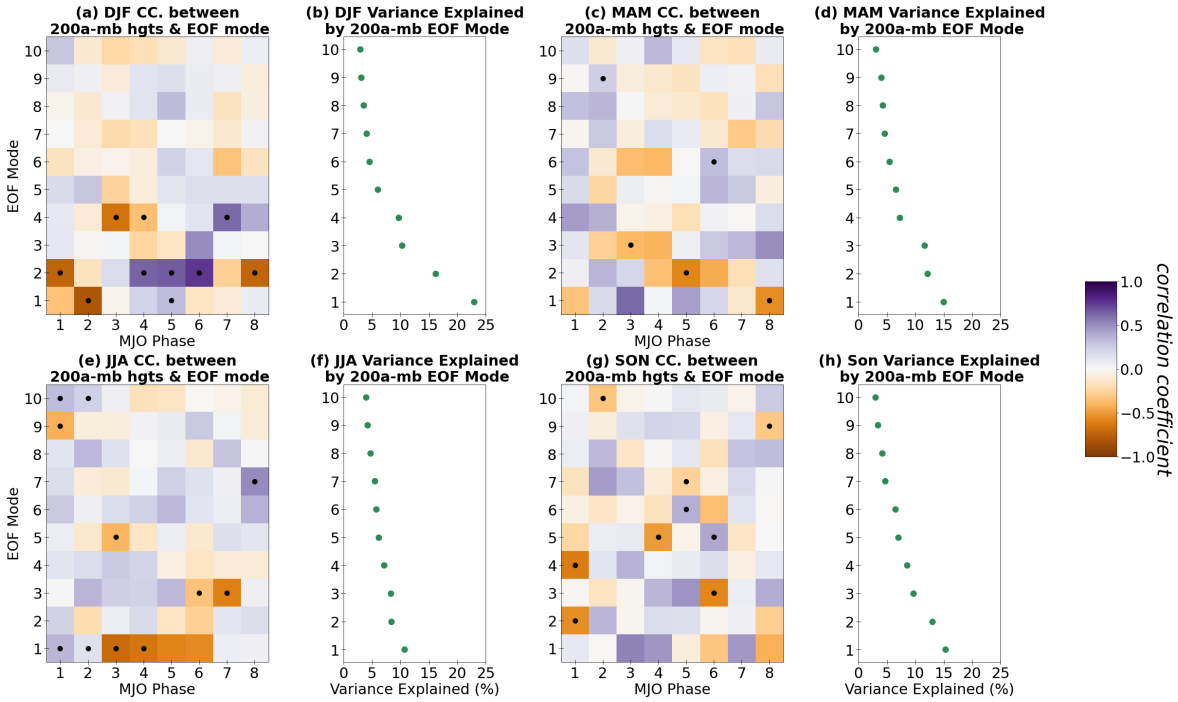

Figure 2.2: Seasonal correlation coefficients between MJO phase 200-mb height anomalies and various EOF modes (Regression of 200-mb height anomalies onto the standardized PC time series of daily mean North Pacific 200-mb anomalous heights (m)) Sub-panel (a) is winter, (b) is the spring, (c) is the summer, and (d) is the fall EOF. The black stipple dots seen denote locations where p<0.1 when using a Monte Carlo test.

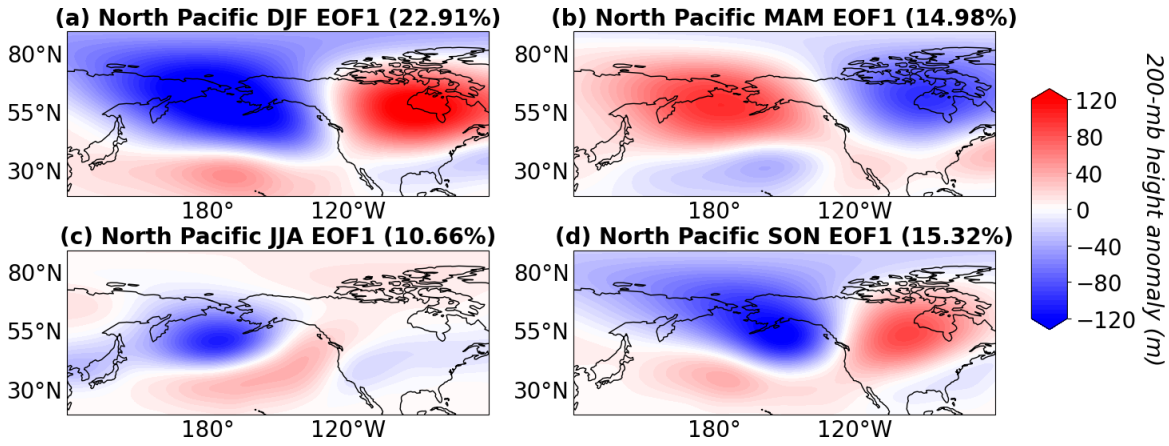

Figure 2.3: Regression of 200-mb height anomalies onto the standardized PC1 time series of daily mean North Pacific 200-mb anomalous heights (m) where the blue shading indicated anomalous lower heights and troughing while the red shading indicates anomalous higher heights and ridging. Sub-panel (a) is winter, (b) is the spring, (c) is the summer, and (d) is the fall EOF1 where the amount of variance explained for each seasonal EOF1 is indicated.

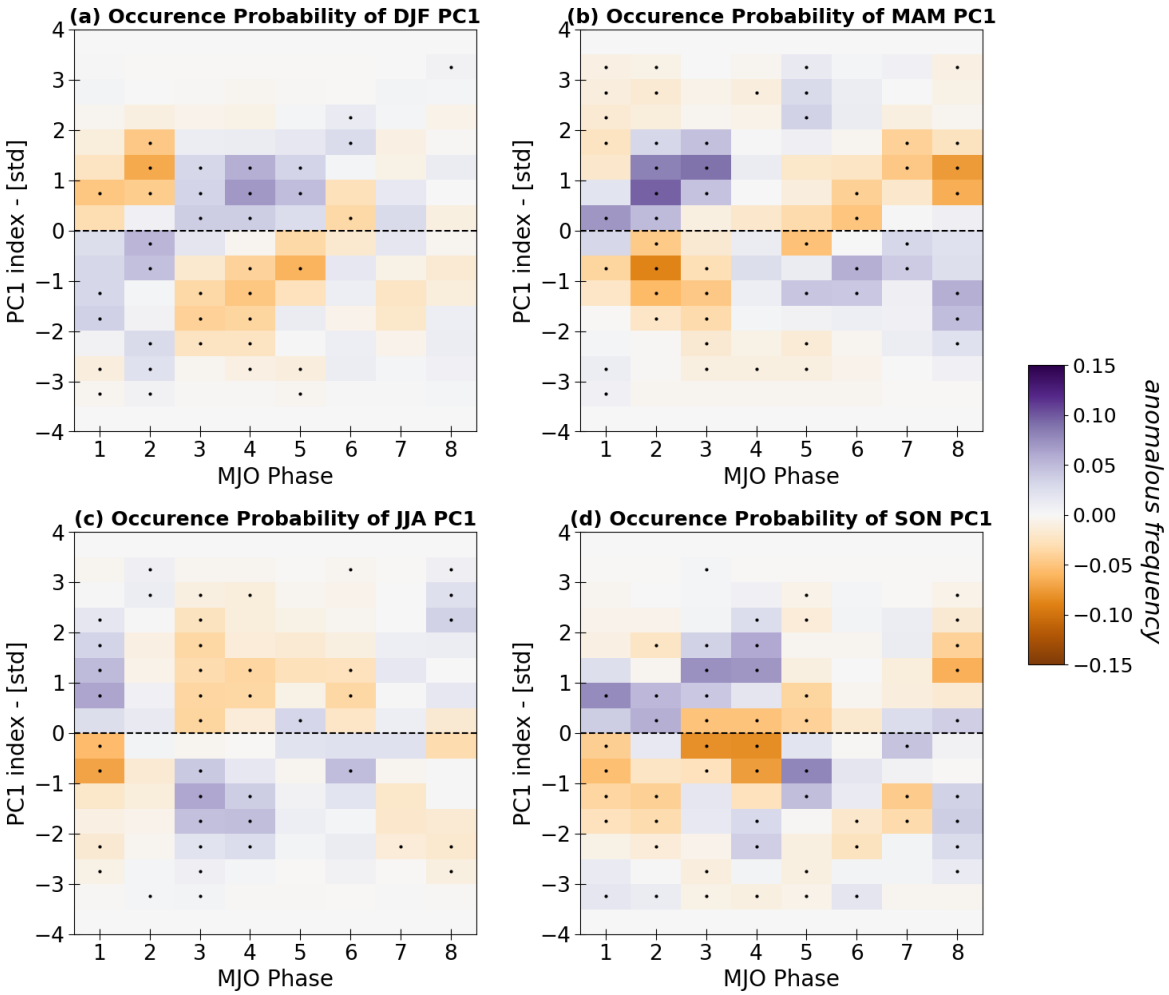

Figure 2.4: Seasonal anomalous probability of occurrence of each season's PC1 which was found doing the EOF analysis where panel (a) is winter, (b) is spring, (c) is summer, and (d) is fall. The color bar indicates anomalous frequency where purple shading indicates the pattern is more likely to occur compared to climatology and the orange shading indicates the pattern is less likely to occur compared to climatology. The black stipple dots seen denote points where $p<0.1$ when using a Monte Carlo test.

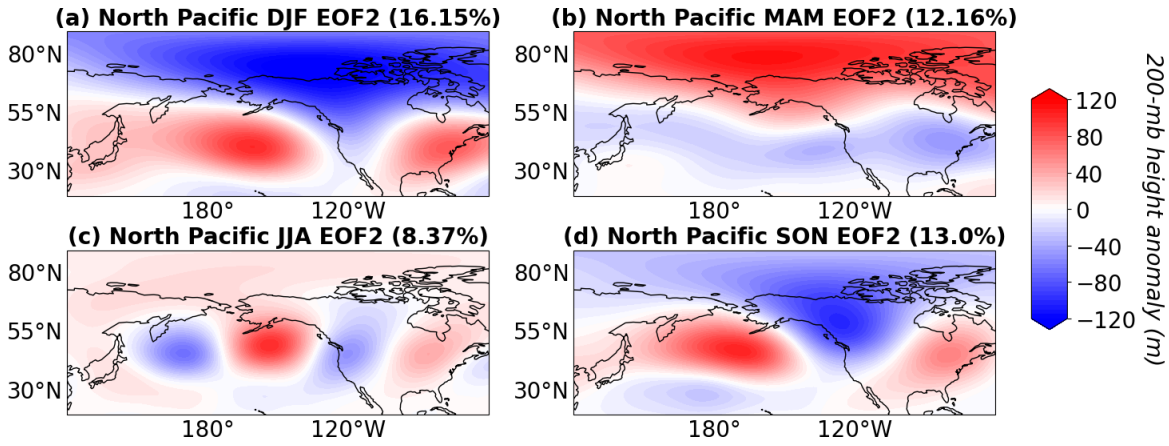

Figure 2.5: Regression of 200-mb height anomalies onto the standardized PC2 time series of daily mean North Pacific 200-mb anomalous heights (m) where the blue shading indicated anomalous lower heights and troughing while the red shading indicates anomalous higher heights and ridging. Sub-panel (a) is winter, (b) is the spring, (c) is the summer, and (d) is the fall EOF1 where the amount of variance explained for each seasonal EOF2 is indicated.

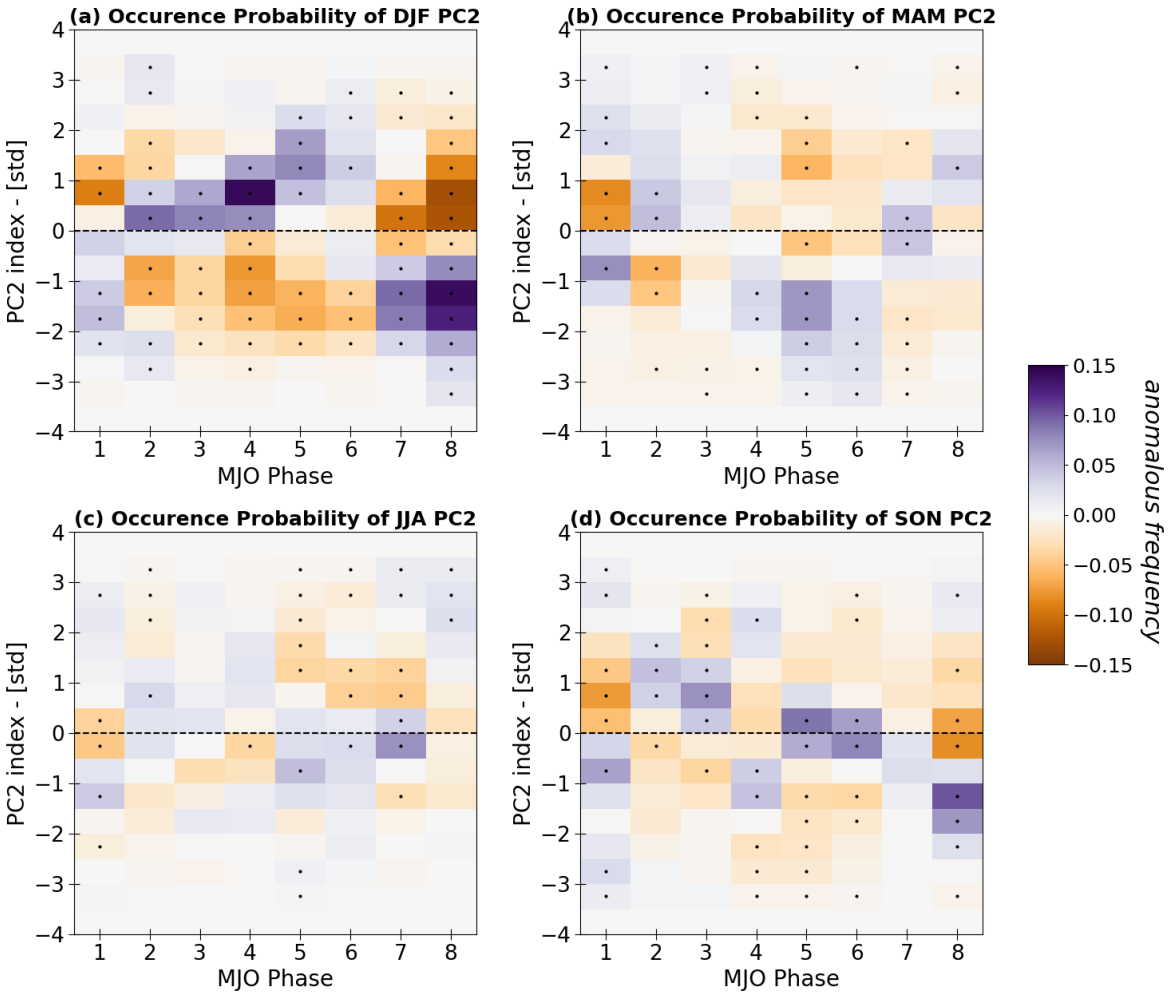

Figure 2.6: Seasonal anomalous probability of occurrence of each season's PC2 which was found doing the EOF analysis where panel (a) is winter, (b) is spring, (c) is summer, and (d) is fall. The color bar indicates anomalous frequency where purple shading indicates the pattern is more likely to occur compared to climatology and the orange shading indicates the pattern is less likely to occur compared to climatology. The black stipple dots seen denote points where $p<0.1$ when using a Monte Carlo test.

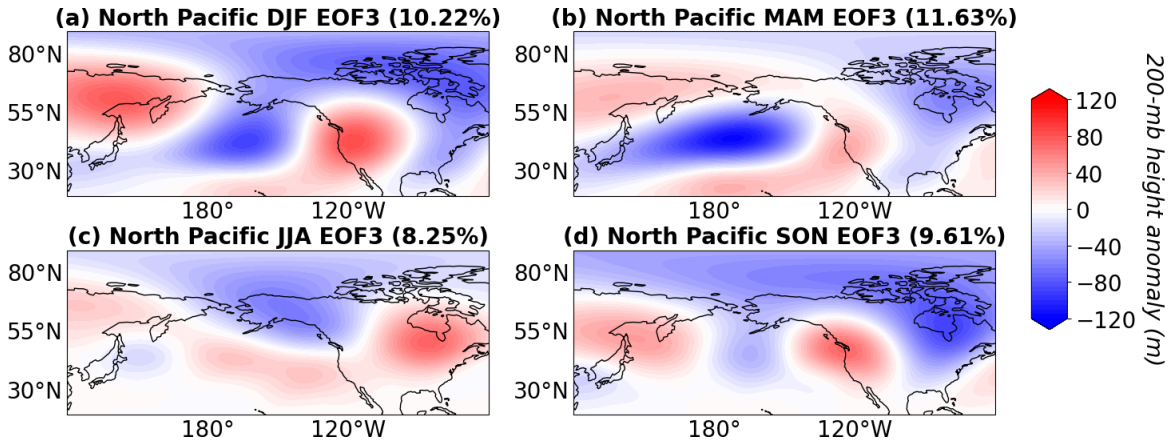

Figure 2.7: Regression of 200-mb height anomalies onto the standardized PC3 time series of daily mean North Pacific 500-mb anomalous heights (m) where the blue shading indicated anomalous lower heights and troughing while the red shading indicates anomalous higher heights and ridging. Sub-panel (a) is winter, (b) is the spring, (c) is the summer, and (d) is the fall EOF3 where the amount of variance explained for each seasonal EOF3 is indicated.

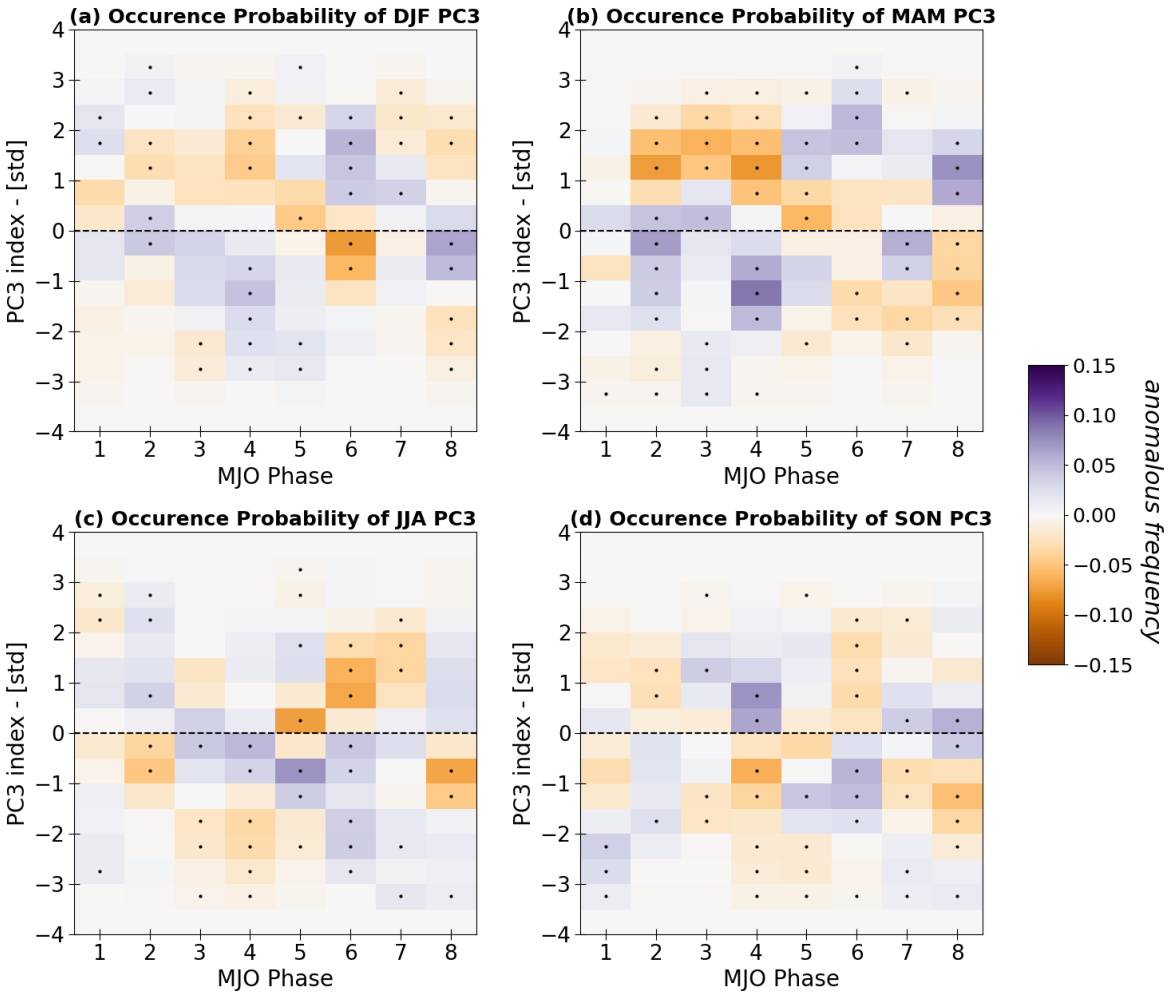

Figure 2.8: Seasonal anomalous probability of occurrence of each season's PC3 which was found doing the EOF analysis where panel (a) is winter, (b) is spring, (c) is summer, and (d) is fall. The color bar indicates anomalous frequency where purple shading indicates the pattern is more likely to occur compared to climatology and the orange shading indicates the pattern is less likely to occur compared to climatology. The black stipple dots seen denote points where $p<0.1$ when using a Monte Carlo test.

Chapter 3

Diagnosis of MJO Seasonal Teleconnections through the Rossby Wave Source (RWS)

The goal of this chapter is to understand why MJO teleconnections have seasonality as shown in Chapter 2. This is done by investigating seasonal changes of MJO-generated Rossby Wave Source (RWS) which is shown to be useful for understanding MJO teleconnections (MORI and WATANABE 2008; Seo and Lee 2017; Tseng et al. 2019). We will look at the seasonal RWS associated with MJO phase, how the produced RWS ties with the EOF patterns shown in Chapter 2, and which processes contribute to the RWS to understand what drives the seasonal differences in the RWS. The analysis that will be presented in this chapter will demonstrate the following main findings:

1. The MJO-generated anomalous RWS varies with both season and phase. In turn, this seasonality helps explain the observed seasonal differences in the MJO teleconnections seen in Chapter 2.

2. The seasonal state of the MJO, rather than the background midlatitude state, has a greater influence on the observed pattern and strength of RWS which differs from the findings of previous studies.

3.1 Definition of the RWS

Many studies like MORI and WATANABE (2008), Seo and Lee (2017), and Tseng et al. (2019) have used the RWS to help explain the formation of teleconnections. Using the RWS allows us to understand the extratropical vorticity that can be produced by tropical heating of the MJO and associated upper-tropospheric divergent flow. The anomalous upper-level divergent flow of the MJO generates the RWS due to its interaction with strong absolute vorticity and the gradient associated with the mid-latitude North Pacific westerly jet (Seo and Lee 2017; Wang et al. 2020). To quantify the RWS, we use the anomalous linearized RWS, RWS', shown in Eqn. 3.1 (Sardeshmukh and Hoskins 1988):

$$RWS' = -\overrightarrow{v_\chi'} \cdot \nabla\bar{\eta} - \overrightarrow{\bar{v}_\chi} \cdot \nabla\eta' - \bar{\eta} \cdot D' - \eta' \cdot \bar{D} \tag{3.1}$$

In Eq. 3.1, $\overrightarrow{v_\chi}$ is divergent flow from the MJO, η is the absolute vorticity, and D is divergence which all are taken at 200-mb. The primes indicate anomalies, the overhead bars indicate seasonal climatology, and ∇ indicates the gradient. The first term on the right-hand side of Eqn. 3.1 is the advection of climatological absolute vorticity by the anomalous divergent wind. The second term is the advection of anomalous absolute vorticity by the climatological divergent wind. The third term is the stretching of climatological absolute vorticity by the anomalous divergence. Finally, the fourth term is the stretching of anomalous absolute vorticity by the climatological divergence. These terms in Equation 3.1 or the RWS' represents that interactions of anomalies and background states are important to the net generation of vorticity. We note that this linearized RWS' does not account for any non-linear processes, and we will discuss the potential importance of nonlinear processes in later sections.

3.2 Data and Methods

As in the previous chapter, we used the OMI to track the location and strength of the MJO. To calculate the anomalous RWS (Eq. 3.1), we used 200-mb horizontal and meridional winds and 200-mb velocity potential from the ERA5 data set. The calculation of absolute vorticity used the 200-mb horizontal winds while the divergent winds were found using the 200-mb velocity potential. Again, the following analysis is done for the same seasons as in Chapter 2: DJF, MAM, JJA, and SON.

To evaluate the produced MJO-generated RWS' pattern, we composited the anomalous RWS by MJO phases for each season. We then examine if the formation of a certain EOF pattern is caused/triggered by the MJO through the generation of the RWS. To do so, we check if the RWS patterns on the days leading up to the formation of the EOF pattern match with the RWS' of the MJO. If their patterns of RWS' match, it then suggests that the generated RWS' of the MJO is conducive to the formation of such EOF. Using the PC time series acquired in the previous chapter, we define days of positive PC as days that had a PC index greater than one and days of negative PC had a PC index less than negative one. Then, we composited the RWS' by days of positive and negative PC. Lagged composites of RWS' were also generated to see the intraseasonal evolution of the RWS associated with PCs. These lagged composites were made on 5, 10, and 15 days prior to the days of identified positive and negative PCs to capture the evolution of MJO phases that typically last around 5 days. To grasp whether the PC-based RWS' is similar to the MJO-based RWS', we regress the PC-based RWS' composite map onto the MJO-based RWS' composite map for each OMI phase and season for the respective lags including Day 0. This was calculated over 0-75 °N and 20°E - 80 °W, the areas where the MJO can generate RWS' that relate to the formation of EOF patterns in the North Pacific.

Error bars (confidence intervals) were found by Monte Carlo simulations with a 1000-iteration re-sampling method with repetitions. Composited days were randomly re-sampled within the season, which were used to recalculate a new composite value. This was repeated 1000 times to generate a distribution and its bottom and top 5% gives the confidence interval. Using the confidence interval, the observed composited value is compared to the interval and has a p-value calculated where if the p-value was a value less than 0.05 or greater than 0.95, it is considered different from zero and it did not occur by chance, so it is deemed significant.

3.3 Results

3.3.1 Seasonal Differences in the MJO-Generated RWS

We first evaluated how the anomalous 200-mb RWS changes seasonally within the MJO phase, which can be demonstrated with Fig. 3.1. When comparing the strength of the RWS seasonally, the strongest amplitude is, again, found in winter. Fig. 3.1c-h show that the amplitude of the RWS decreases in other seasons with the weakest RWS' in summer. It also shows that the zonal extent of the RWS' varies by season.

This seasonal difference in RWS' can be understood through the anomalous divergent winds tied with the MJO and the North Pacific Westerly Jet's (NPJ) absolute vorticity, two components that change seasonally. This can be visualized with Fig. 3.2, a seasonal composite of the mean absolute vorticity with phase 4 and 8 anomalous divergent winds associated with the MJO. The meridional gradient of absolute vorticity is the sharpest in winter off the eastern Asian coast. Fig. 3.2b-d shows the sharpness of the meridional gradient decreases in strength in the other seasons and is weakest in summer. So, there is seasonality in the jet and its associated absolute vorticity gradient. We can also compare the strength of anomalous divergent winds connected with

MJO and how that changes seasonally. Comparing phase 4 of the MJO seasonally, Fig. 3.2a-d, the strength and direction of the divergent winds change with seasons. This is also visualized with phase 8 of the MJO in Fig. 3.2e-h. The observed seasonality in the RWS' can be tied to the seasonal variability in MJO's divergent winds and the NPJ's absolute vorticity.

The produced MJO-generated RWS' is not necessarily the exact opposite even when tropical precipitation anomalies switch their sign between phases 4 and 8 of the MJO. In spring phase 4, Fig. 3.1c has a strip of negative RWS' that zonally extends from the eastern edge of India to the eastern coast of China. Fig. 3.1d, phase 8 in spring, has a more northwestward-tilted strip of positive RWS' in the same area. Furthermore, when comparing Fig. 3.2a and e (DJF and JJA of MJO phase 4), there are stronger divergent winds over the eastern Asian continent in phase 4 compared to slightly weaker (convergent) winds in the same area during phase 8. This could possibly explain why these two phases do not produce exactly opposite RWS' and could possibly help explain why earlier phase 4 and 8 did not produce opposite PC patterns in Chapter 2.

These seasonal differences in the generated RWS' can be connected to the documented PC patterns in our previous chapter. Previous studies suggested that the MJO-generated anomalous RWS is where the waves that enter the PNA region originate from (Seo and Lee 2017). If the RWS' changes seasonally, then it is going to change the produced teleconnection pattern seasonally and can possibly explain the seasonality in the MJO teleconnections.

3.3.2 Seasonal Connections between MJO-Generated RWS and the Formation of Extratropical EOF Modes

This section will demonstrate that the extratropical EOF modes that are strongly related to the MJO result from the generation of the RWS' by the MJO while the EOF modes that are weakly related to the MJO may form different sources of Rossby waves. To demonstrate this, we investigate the RWS' pattern leading up to the EOF pattern and compare its similarity to the MJO-based RWS' composites.

3.3.2.1 First EOF Modes of the Seasons

Chapter 2 indicates that winter and summer are the two seasons to be strongly correlated with EOF1 where the relationship can be possibly explained through the generation of a RWS'. We can first look at the seasonal lagged composites of the RWS' on Day-0 and 10 days before the days of positive PC1 with Fig. 3.3. The definition of the positive and negative PC days are described in section 3.2. Lags are defined as the days before a PC day occurs. While 3 different lags were examined, we present only Day 0 and Day -10 as Day -15 had no strong RWS' patterns, and Day -5's RWS' is very similar to Day 0. On Day 0 of the positive PC1, we can see seasonal differences in the RWS' pattern in the strength and position of the areas of RWS' in Fig. 3.3a-d. Winter and fall have similar RWS' strength with differences in the size of the negative RWS' over the northeast Pacific and the positive RWS' surrounding it. This coincides with the seasons' EOF1 patterns (Fig. 2.3) found in Chapter 2 with the ridges and troughs aligning with the negative and positive RWS' respectively but shifted eastward. In contrast, spring has an opposite pattern to winter positive PC1 RWS' just like how spring's EOF1 pattern was opposite to the other seasons where the area positive RWS' is to the west of the EOF1's trough. It is worth noting that the corresponding areas

of positive RWS' differ slightly seasonally and could imply that their role is important to how the height patterns develop.

The negative PC1 has RWS' patterns that are similar but opposite to the patterns of the positive PC1. The negative PC1 RWS' pattern is demonstrated with Fig. 3.4. Day-0 of the negative PC1 again demonstrates seasonal differences in the produced RWS'. Winter and fall are similar in magnitude, but winter's positive RWS' extends from Alaska to Northern California whereas fall is confined to Alaska and western Canada. These RWS' centers can be tied to the EOF1 patterns (Fig. 2.3) and are aligned with the areas of troughs and ridges but shifted westward. Spring, in contrast, has weak negative RWS' over the northeast Pacific and lines up with the ridge in its EOF1 pattern. Once more, we see the positioning of the negative RWS' (positive for spring) differs in each season from being either a band from the northwest wrapping around to the south, just south, northwest and directly west.

Among these seasonal PC1s, the ones that are strongly tied to the MJO show a developed RWS' over the NPJ region preceding the formation of the PC1 pattern. The days leading up to a positive PC1 day, there are seasonal differences in the produced RWS' (Fig. 3.3e-h). Figure 3.3 indicates there is no propagation of the RWS, seasonally, rather it seems to develop locally on a timescale of less than 10 days. This could be the reason why the MJO is not strongly tied with the formation of the PC1 in spring and fall. Although, there is a sign of a strong zonally-extended negative RWS over East Asia at -10 days of the positive PC1, exclusively in winter. A similar signal over East Asia occurs 10 days before the negative PC1 forms, with a positive RWS' over the area. This might explain why the MJO is only more related to PC1 during winter exclusively. While weaker in summer, there is a signal of positive RWS over Korea 10 days before the positive PC1 formation and could also be the reason that JJA is more related to PC1.

The PC1s that are tied to the MJO have a quantifiable similarity between the produced PC1 RWS' and the MJO's RWS'. To better quantify the similarity of these RWS' patterns associated with PC1 and different phases of the MJO, we regressed the composite maps of PC-based RWS' to the ones of MJO-based RWS', and the obtained regression coefficients are shown in Fig. 3.5. Figure 3.5a indicates a strong regression coefficient 10 days before the positive PC1 formation in winter indicating that the positive PC1's RWS looks like the MJO's RWS in phases 3 and 4. A stepping pattern is also apparent where the positive regression coefficients shift to the higher phase of the MJO with time. Comparing Fig. 3.3a and Fig. 3.1a, the zonally-extended negative RWS' over the eastern Asian continent by the NPJ region is evident in both figures where the PC's RWS 10 days before is weaker than the MJO's RWS. Similarly, there is a slight stepping pattern in summer and fall. In contrast, no clear patterns are portrayed between the negative PC1 RWS' and MJO's RWS. The lack of correspondence between the MJO and PC1's RWS' can help explain the weak relationships between the MJO and the PC1/EOF1 pattern in most seasons. The summer MJO, however, was shown have a stronger relationship than other seasons with the PC1 pattern indicated with Fig. 2.2e in Chapter 2. It is possible that the RWS' is not capturing the mechanisms by which the MJO generates the summer PC1 pattern and this could be due to the absence of non-linear processes like up-scale feedbacks from synoptic variability.

3.3.2.2 Second EOF Modes of the Seasons

The strength of the positive PC2 RWS' can be linked to the strength of the relationship between the MJO and the PC2 pattern. Examining the positive PC2 and associated RWS' with Fig. 3.6, we emphasize the seasonality in the RWS' produced, in strength and positioning on Day 0. As discussed in Chapter 2, PC2 is most strongly related to the MJO during winter when the MJO has the strongest generated RWS'.

Winter has a small, strong positive RWS' over the northeast Pacific and a negative RWS' over the east Asian continent. This coincides with the troughs and ridges in the EOF2 pattern (Fig. 2.5a) but the RWS' are shifted westward. The positive PC2 RWS' in summer and fall are of similar magnitude and mimic their EOF2's trough and ridges with the RWS' shifted off-centered. Spring's positive PC2 has no defined RWS' areas and indicates the development of the spring EOF2 is not from the linearized RWS but from another source.

The MJO is tied to the negative PC2 pattern when a strong RWS' is developed. Again, the RWS' produced is opposite to the positive PC2 RWS' pattern. Figure 3.7 shows the produced RWS' of the negative PC2 index, and at Day-0, there are seasonal contrasts in the produced RWS'. Winter and fall, Fig. 3.7a and d, are similar in strength with differences in positioning. However, the biggest difference between the two seasons is the strong dipole RWS' generated over the NPJ region in winter. Again, this can explain why the winter MJO is more strongly tied to its PC2 pattern. Comparing the produced RWS' with their respective EOF2, in winter and fall, they have similar positions where again the RWS' centers are shifted westward. Summer has the opposite pattern found in its positive PC2 RWS' and correspondence again with the ridges and troughs in the EOF2 pattern (Fig. 2.5c). The lack of significant RWS' in spring is again evident for the negative PC2 pattern. With the lack of generated RWS' for both the positive and negative PC2 pattern in MAM, it begs the question on the pathway on how the MAM teleconnection can form if not from a RWS'. Due to the RWS' being linearized, it neglects any non-linear processes that can be in play which could be the formation mechanism of spring teleconnection. For example, synoptic scale variability could be feeding back to the longer, intraseasonal periods to generate the MJO teleconnection. Further analysis would be needed to answer this.

With the seasonal PC2s, the ones more tied to the MJO have a weaker RWS' anomaly over the northeast Pacific. At 10 days prior to the formation of the positive PC1 (Fig. 3.6e-h) winter and fall have present RWS' anomalies that are in the same area as Day 0 but weaker. Spring has a weak positive RWS' over the NPJ and summer has no prominent RWS' 10 days before the positive PC1 pattern. For the positive PC2 pattern, Fig. 3.6 indicates that the RWS' develops and persists on a timescale of 10 days (and greater). With the negative PC2 pattern (Fig. 3.7e-h), there are no dominant RWS' patterns apparent 10 days prior to its formation, except for winter. The winter has a negative RWS' in the same location as its Day 0 RWS' pattern. This could indicate the strong relationship between the MJO and the PC2 pattern is tied the formation of a RWS' over the northeast Pacific especially in winter.

A quantifiable similarity between the MJO RWS' and PC2 RWS' explains the strong relationship between the MJO and PC2 pattern. Regression coefficients between the PC2 RWS' and MJO RWS' are shown in Fig. 3.8. Due to the strong relationship with PC2 and the winter MJO presented in Chapter 2, the larger magnitude of regression coefficients in Fig. 3.8a and e coincide with those results. This suggests that the winter MJO is more strongly tied to the formation PC2 through the generation of its RWS'. It is likely that the PC2 pattern is the PNA, which the MJO is known to generate 30% of PNA events (MORI and WATANABE 2008). The RWS' development of the winter PC2 pattern is consistent with (MORI and WATANABE 2008)'s work, as they indicate a RWS' over the NPJ and northeast Pacific 9 days prior to a positive PNA pattern and a RWS' over the northeast Pacific for the negative PNA.

For the positive PC2 in winter, a stationary pattern is apparent where the positive regression coefficient persists with the same MJO phase. In winter, the regression coefficients begin to increase around Day -10 and Day -5 during MJO phases 2 to 5 for the formation of the positive PC2 pattern. By comparing the MJO RWS' composite

with the Day -10 positive PC2 RWS', both have a positive RWS' present over the northeast Pacific. The regression coefficients in fall are strong all throughout phase 2 of the MJO with a stationary pattern present. In contrast, both winter and fall's negative PC2 pattern has a mixture of a stepping and stationary pattern. In fall, the regression coefficients begin to increase on Day -5 during phase 2 of the MJO and Day -10 during phase 7 of the MJO. Winter's regression coefficients peak Day -5 of negative PC2 formation. With differences in the positive and negative PC2 showcasing a stationary or stepping pattern can have implications on the mechanisms by which the MJO generates them. For the RWS' to persist for 15 days, the MJO needs to be slow-moving to keep the RWS' in the same place whereas the stepping pattern indicates the propagation of the RWS' with the MJO. Such a slow-moving MJO could occur more frequently with a La Niñaa or Quasi-Biennial Oscillation easterlies as documented by previous work (Pohl and Matthews 2007; Song and Wu 2020). In spring, both PC2 patterns have very weak stepping patterns and the lack of a generated RWS' could possibly explain the weak relationship between PC2 and the MJO. Lastly, the summer's PC2 RWS' has no similarity to the MJO RWS' which explains the lack of the relationship between the two.

3.3.2.3 Third EOF Modes of the Seasons

As indicated in Chapter 2, the spring MJO is most strongly tied to the PC3 pattern which can be explained by the generation of a strong RWS' compared to the PC1/2 RWS' in spring. The RWS' associated with the positive PC3 index is illustrated with Fig. 3.9 where spring and winter have similar, strong RWS' patterns produced. The negative RWS' in both is generated over the east-central Pacific where it is meridionally extended in winter while it is zonally extended in spring. Winter and spring's RWS' align with the troughs and ridges in their EOF3 (Fig. 2.7) patterns but shifted

northwestward. The elongated RWS' in spring can be tied to the elongated troughs and ridges in the EOF3 pattern. However, as indicated in Chapter 2, the winter MJO is not tied with the PC3 pattern even though a strong RWS' is produced, indicating the RWS' is important for its formation but it is not MJO-generated. In contrast, spring is tied to the PC3 pattern with a prominent RWS' pattern.

These same findings, with opposite RWS' patterns from the positive PC3, can be visualized with the negative PC3 index in Fig. 3.10. At 10 days before the formation of the positive spring PC3 pattern, an area of weak positive RWS' is generated near the NPJ region and negative RWS' over the northeast Pacific depicted in Fig. 3.9f. However, for the negative PC3, 10 days prior to its development, there is only weak positive RWS' over the northwest Pacific. The differences in the two RWS' patterns produced for PC3 formation could indicate that the relationship between the MJO and the sign of PC3 differs in mechanisms.

Even if a strong RWS' is developed, the MJO is only tied to the PC3 with RWS' patterns that look similar to the MJO-generated RWS'. We quantify the similarity via regression coefficients between the PC3 RWS' and MJO RWS' demonstrated in Fig. 3.11. In spring, there are higher amplitudes of regression coefficients (dark shading) which is consistent with results from Chapter 2. The positive PC3 has a slight stepping pattern of its regression coefficients that becomes stationary at Day -5 and after around phases 7 and 8 of the MJO. Regression coefficients peak at Day 0 and are weakest at Day -15. Comparing the OMI RWS' with the positive PC3 RWS' (Fig. 3.1 and Fig. 3.9b and f), all three composites have a positive RWS' over the NPJ where the PC3 RWS' does not extend all the way to the east coast of India. In contrast, the positive regression coefficients for the negative PC3 in spring exhibit a stationary pattern over 15 days during phases 2 to 4 of the MJO. Again, the coefficients at Day 0 have the strongest regression coefficients during phase 3 of the MJO. While the phase 3 composite is not

shown, the MJO phase 3 RWS' has an negative RWS' over the NPJ similar to Day 0 of the negative PC3. Furthermore, 10 days before the formation of the negative PC3, the negative PC3 RWS' and MJO RWS' during phase 3 have off-centered but coinciding areas of positive RWS'. Winter PC3 had a strong RWS' generated but regression coefficients between the MJO and PC3's RWS in Fig. 3.11# only have similarity on Day 0. This would indicate that the RWS' needed for the formation of PC3 is less tied to the MJO. In spring, since the positive PC3 has a mixture of a stepping and stationary pattern whereas the negative PC3 has a stationary has implications on how the MJO is tied to the PC3 pattern and the mechanisms for the MJO to generate the patterns.

Altogether, the relationships between the MJO and the seasonal PC patterns can be explained due to both the seasonal differences in the generated RWS' and whether the PC's RWS' is similar to the MJO. The existence of the strong RWS appearing only 10 days before the formation of EOF patterns indicates that these EOF patterns develop on such timescales. These seasonal differences imply that in order to accurately represent and produce MJO teleconnections, an accurate representation of the RWS' is crucial. In order to simulate the RWS' correctly, we need accuracy in both the background state and divergent winds.

3.3.3 Diagnosis of Contributing Processes to RWS

Previous studies like Seo and Lee (2017), MORI and WATANABE (2008), and Sardeshmukh and Hoskins (1988) have indicated that the terms that have climatological divergent wind (term 2 and 4 in Eqn. 3.1) are much smaller and have little contribution to the MJO-generated RWS'. Rather, those studies suggest that the interactions of anomalous divergent winds linked to the MJO with the background vorticity are more important. However, those previous studies were limited to boreal winter,

therefore, an understanding of what terms of Eqn. 3.1 (and processes) contribute to the seasonal RWS' most dominantly is needed. To answer that, we found the seasonal term contribution to the MJO-generated RWS' for each MJO phase. The contribution was calculated over a boxed domain of 20-45 °N and 90-120 °E, which is the area where the MJO generates its greatest RWS' indicated in Fig. 3.1. The contribution was found with the following formula:

$$\text{Contribution Value} = \frac{\sum \text{Term\#} * \text{RWS}}{\sum \text{RWS}^2} \tag{3.2}$$

The quantification of what processes (or terms in Eqn. 3.1) generate the RWS' is portrayed in Fig. 3.12 where term 1 is the blue line with circles, term 2 is the orange line with upside-down triangles, term 3 is the green line with triangles, term 4 is the red line with diamonds, and addition of term 1, 2, and 4 is the purple lines with plus signs. By adding term 1, 2, and 4, this helps with quantifying how these processes together compare to the most dominant term. The color shading indicates the confidence interval of the term's contribution and was found with Monte Carlo simulations. Here, when re-sampling the days, the random pool is confined to the respective phase days.

It is apparent from Fig. 3.12 that the most dominant term/process is term 3, the stretching of climatological absolute vorticity by the anomalous divergence associated with the MJO, in all seasons due to its high contribution values. Due to existence of the strong NPJ and associated vorticity, a region of higher-value vorticity appears closer to the equator in winter, visualized in Fig. 3.2, contributing to the greater stretching of the vorticity. This indicates that the strongest RWS' patterns are generated because of the strength and location of NPJ allowing for the divergence associated with the MJO to cause a stronger generation of vorticity via stretching which supports the work of

Song and Wu (2020) and disagrees with MORI and WATANABE (2008); Seo and Lee (2017).

While the contribution of term 3 is most dominant in all seasons, it can fluctuate with MJO phases in winter. Term 3 includes anomalous divergence associated with the MJO and yet we have a sudden drop in contribution value in phase 4 in winter. This does not necessarily indicate that term 3 decreases in magnitude. Instead, it may highlight the presence of the MJO-associated divergent winds at the same location of the NPJ and its associated gradient in absolute vorticity leading to strong advection of absolute vorticity. In winter, Fig. 3.12a indicates term 1 and term 3 can have equivalent contributions in some phases, unlike the rest of the seasons. The MJO has its' strongest convection in winter, in turn has its' strongest associated anomalous divergent wind and divergence which are included in these terms hence the terms' similar magnitude.

The other terms seem to have variability in their contribution. Term 1, the advection of climatological absolute vorticity by the anomalous divergent wind associated with the MJO, has a rather consistent contribution in each season with two peaks occurring during precipitation opposites like phase 4 and 8 or phase 1 and phase 5. This implies that the absolute vorticity gradient and divergence/convergence both occur strongly over the same region, in these phases, leading to a stronger contribution of term. This happens, most likely, because of MJO-associated divergent winds coinciding over the region of the strongest subtropical jet in the western Pacific.

The advection of anomalous absolute vorticity by the climatological divergent wind, term 2, also has rather a consistent contribution seasonally. Term 2 seems to have its greatest contribution during the summer season. It could be possible that there is some influence from the summer monsoon over India that strengthens the climatological divergent wind patterns during this time. Further analysis would be needed to support this claim.

Finally, term 4 seems only to contribute during the winter and spring season with its greatest contribution in winter. Term 4 has a similar contribution to terms 1 and 2 with its peak in phases 1 and 4 (close but not quite precipitation opposites). The MJO is strongest in winter leading to a greater value of anomalous absolute vorticity to be stretched by the climatological divergent winds allowing a greater contribution value.

Previous studies (Seo and Lee 2017; MORI and WATANABE 2008; Sardeshmukh and Hoskins 1988) have indicated that terms 2 and 4 of Eqn. 3.1 could be ignored and terms 1 and 3 were dominant. However, seen with Fig. 3.12, it can be said that term 3 is dominant yet terms 1, 2, and 4 have too similar and non-negligible magnitude depending on the season. Due to the analysis being confined to this small sub-domain, it is possible that contributions have regional sensitivities. However, even with extending the longitudinal extent of the domain to 60-180 °E, we still see the dominance of term 3 in generating the seasonal RWS' (not shown) indicating consistency throughout different regions. The results emphasize the importance of being able to accurately represent the MJO and background state in simulations as both would contribute seasonally to improving MJO teleconnections modeling.

3.3.4 Relative Sensitivity of RWS to Seasonal MJO Anomalies and Background State

Figure 3.12 and Henderson et al. (2017) showed that both MJO-related anomalies and the background state are in important in generating the amplitude and structure of the observed RWS'. Due to the known seasonality in both, we want to test the sensitivity of the RWS' to the seasonal state of the two by replacing either component with annual-average values. Swapping the components with annual-average values will

help us to understand how much the RWS' is influenced/changed by the seasonal state of the MJO and background state. To achieve this, we calculated two new RWSs: a RWS that would be generated from annual-average MJO phase values and the seasonal background state along with an RWS from the seasonal MJO-related anomalies and an annual-average background state. The annual-average MJO anomalies were calculated for each phase of the MJO by compositing the identified days of each phase from all seasons. With these new RWSs, we will be able to examine how much the observed RWS changes if the season-specific MJO anomalies are replaced by their annual-mean values while retaining the same seasonal background and vice versa. The equations of these new RWSs are as follow:

$$\text{RWS'}_{\text{Annual MJO}} = -\overrightarrow{v'}_{\chi,OMIAnn.} \cdot \nabla\bar{\eta}_{season} - \overrightarrow{\bar{v}}_{\chi,season} \cdot \nabla\eta'_{OMIAnn.} - \bar{\eta}_{season} \cdot D'_{OMIAnn.} - \eta'_{OMIAnn.} \cdot \bar{D}_{season} \quad (3.3)$$

$$\text{RWS'}_{\text{Annual Background}} = -\overrightarrow{v'}_{\chi,OMIseason} \cdot \nabla\bar{\eta}_{BackgroundAnn.} - \overrightarrow{\bar{v}}_{\chi,BackgroundAnn.} \cdot \nabla\eta'_{OMIseason} - \bar{\eta}_{BackgroundAnn.} \cdot D'_{OMIseason} - \eta'_{OMIseason} \cdot \bar{D}_{BackgroundAnn.} \quad (3.4)$$

After calculating the RWS' with Eqn. 3.3 and Eqn. 3.4, we composited each conditional RWS' by MJO phase for each season. With these composites, we can compare these RWSs to examine which component, the seasonal MJO or background state, plays a more important role in generating the observed RWS pattern. To quantify the influence of the seasonal state of the background and MJO, we calculated the correlation coefficients between the original RWS and the two RWS that include annual values.

Figure 3.13 shows a seasonal composite of Eqn. 3.1, Eqn. 3.3, and Eqn. 3.4 for MJO phase 4. The left column of Fig. 3.13 indicates the observed RWS', the middle column shows RWS'$_{\text{Annual MJO}}$, and the right column shows RWS'$_{\text{Annual Background}}$. If RWS'$_{\text{Annual MJO}}$ changes significantly from the observed RWS', it indicates that retaining the seasonal state of the MJO plays a dominant role in generating the observed RWS'. While if RWS'$_{\text{Annual Background}}$ differs significantly from the observed RWS', then retaining the seasonal background state plays a dominant role.

Figure 3.13 shows that the seasonal state of the MJO has a great influence in creating the observed RWS' pattern in all seasons. For example, during winter, retaining MJO winter seasonality only (Fig. 3.13c) generates most to all of the observed RWS' spatial pattern over the entire domain in Fig. 3.13a whereas retaining the background seasonality ((Fig. 3.13b) generates its RWS' over the NPJ region. The stronger dependence of the RWS' to the background state over the NPJ indicates the jet contributes strongly to the generation of RWS' there. For each season and its three panels, we continue to see the MJO seasonality dominates in generating the actual RWS' spatial scale. A similar analysis was done for phase 8 of the MJO which can be seen with Fig. 3.14 and yields the same results as interpreted as above. We can see that the seasonal MJO state has a dominant role in producing the observed RWS', both spatially and in magnitude. This differs from previous studies like Henderson et al. (2017) where it was concluded that the background state would play a bigger in the generation of the RWS'.

To support our qualitative assessment from Figs. 3.13–3.14, we quantify how much the seasonal MJO and background state contribute to the observed RWS' pattern. This was done by calculating the seasonal pattern correlation coefficients between the OMI composites of observed RWS' and RWS'$_{\text{Annual Background}}$ or RWS'$_{\text{Annual MJO}}$. This was done for different regions: the whole plotted domain and the NPJ region (The

sub-domain region used in subsection 3.3.3, 20-45 °N and 90-120 °E). Calculating correlation coefficients for these two regions will allow us to understand what seasonal state influences the full RWS' spatial pattern and the RWS' spatial pattern over the NPJ, respectively. Quantification of similarity is visualized in Fig. 3.15 where the greater the correlation coefficient value is to one, the more alike the two pattern look whereas when the correlation coefficient is smaller and closer to zero indicates the spatial patterns lack similarity.

Figure 3.15 illustrates that, again, in each season, the retained MJO seasonality (Annual Background; the orange line with upside-down triangles) is more important and nearly has a correlation coefficient of 1 in all MJO phases. The retained background state seasonality (Annual MJO; blue line with circles) has a high correlation as well but it is farther separated from the orange line. However, for the sub-domain region, the correlation coefficients between the two (green line with triangles and red line with diamonds) are not as separated as when quantified over the whole domain. The sub-domain region encompasses the NPJ region, indicating the seasonal background state is more or equally important than the seasonal state of the MJO. Something worth noting about the sub-domain retained background seasonal state in each season, besides summer, has a decrease in correlation at phase 5 of the MJO meaning that the seasonality of the MJO has a particularly stronger role than the seasonal background state during this phase of the MJO to generate the observed RWS pattern. Again, however, the sub-domain region of retained MJO seasonality still has the greater correlations in all seasons. This highlights that both the seasonal variations in the background and MJO state in the sub-domain domain, do their part in generating the observed RWS' pattern. However, the seasonal state of the MJO seems to have more influence in producing the observed RWS' spatial pattern as a whole.

3.4 Summary

To summarize this chapter, we made the following key findings

1. It was found that the MJO-generated RWS' has strong seasonal variability which in turn explains why certain teleconnection patterns are strongly associated with the MJO.

2. We found that the dominant term/process in generating the RWS' is term 3 or that the location of the subtropical jet being closest and strongest during DJF allows for the divergence associated with MJO to cause the strongest generation of vorticity via stretching.

3. The work here illustrates the seasonal state of the MJO has the most influence in producing the observed RWS' magnitude and spatial pattern.

With these findings come implications on what they mean for the field. First, we mention that a caveat of this study is the lack of inclusion of non-linear processes where previous studies (MORI and WATANABE 2008; Tseng et al. 2019) have shown and indicated that non-linear processes have an important role when it comes to generating teleconnections. Non-linear processes could mean that the MJO modulates the synoptic variability behavior that feedback to the intraseasonal timescale to generate its teleconnections. Further analysis is needed to understand the seasonal role of non-linear processes in generating MJO teleconnections. With our results, there is disagreement between prior literature (MORI and WATANABE 2008; Seo and Lee 2017)(in support of Song and Wu 2020) on which terms/processes are important for the generation of the RWS' where we found there is greater importance of the stretching of vorticity rather than advection of vorticity. This implies that in order to simulate MJO teleconnections more accurately, the representation of the seasonal MJO and background state needs

to be better. Lastly, previous studies (Henderson et al. 2017) highlights the importance of the background state in generating the RWS' as the weak simulation of the MJO had little impact on changes in the RWS'. However, the work here rather illustrates the seasonal state of the MJO has the most influence in producing the observed RWS' both magnitude and spatial pattern. Again, this emphasizes the significance of being able to simulate the MJO characteristics accurately in all seasons to then model MJO teleconnections accurately.

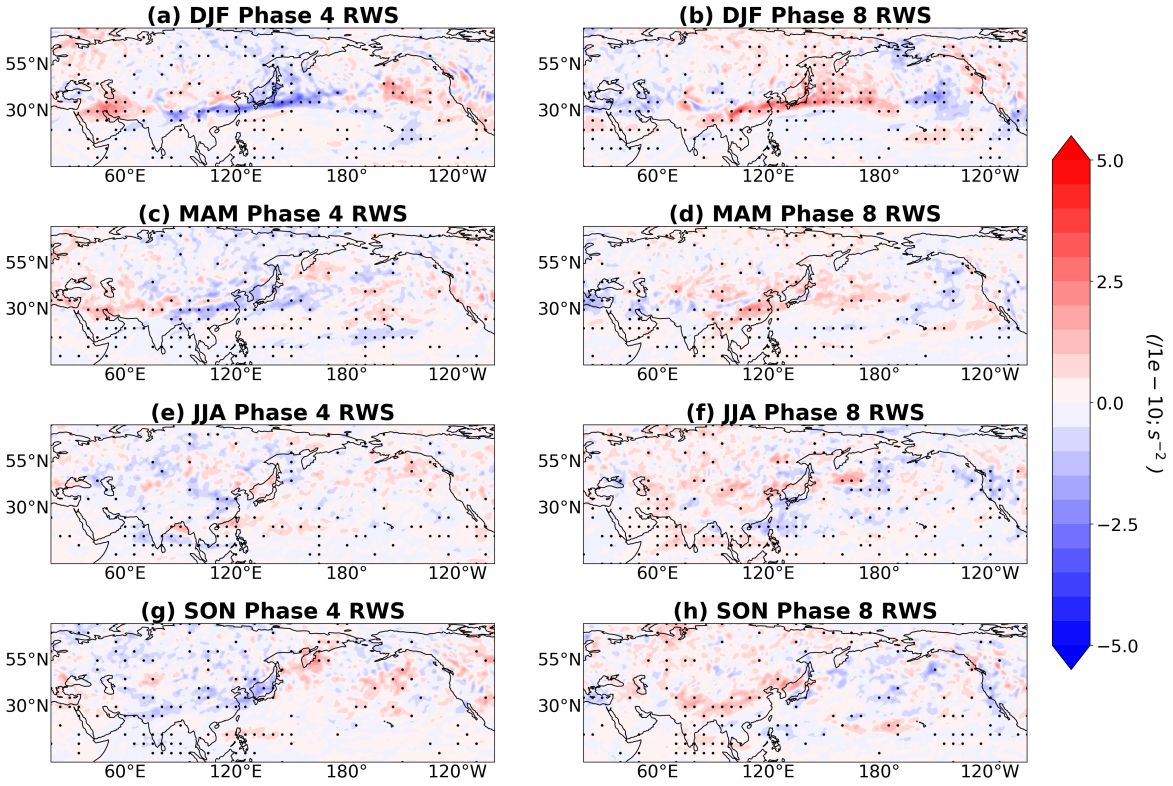

Figure 3.1: Subplotted seasonal OMI composites of anomalous 200-mb RWS generated from the MJO . The figure includes phase 4 and 8 of the MJO where panels (a,b) are winter, (c,d) are spring, (e,f) are summer and (g,h) are fall respectively. The black stipple dots seen denote locations where p<0.1 when using a Monte Carlo test.

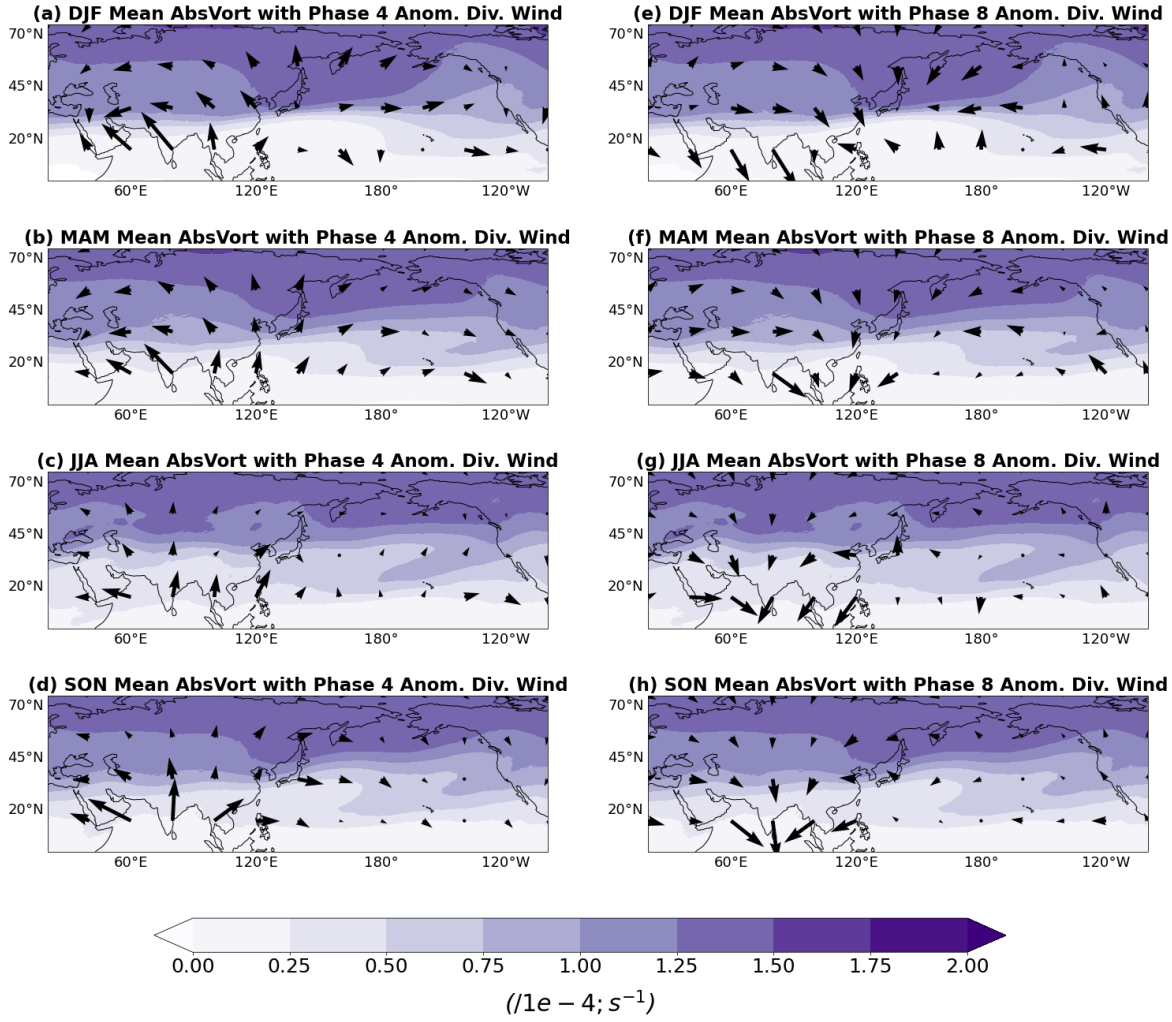

Figure 3.2: Subplotted seasonal composite of climatological (1981-2010) absolute vorticity. The figure includes the anomalous divergent winds from phase 4 and 8 of the MJO where panels (a,e) are winter, (b,f) are spring, (c,g) are summer and (d,h) are fall respectively.

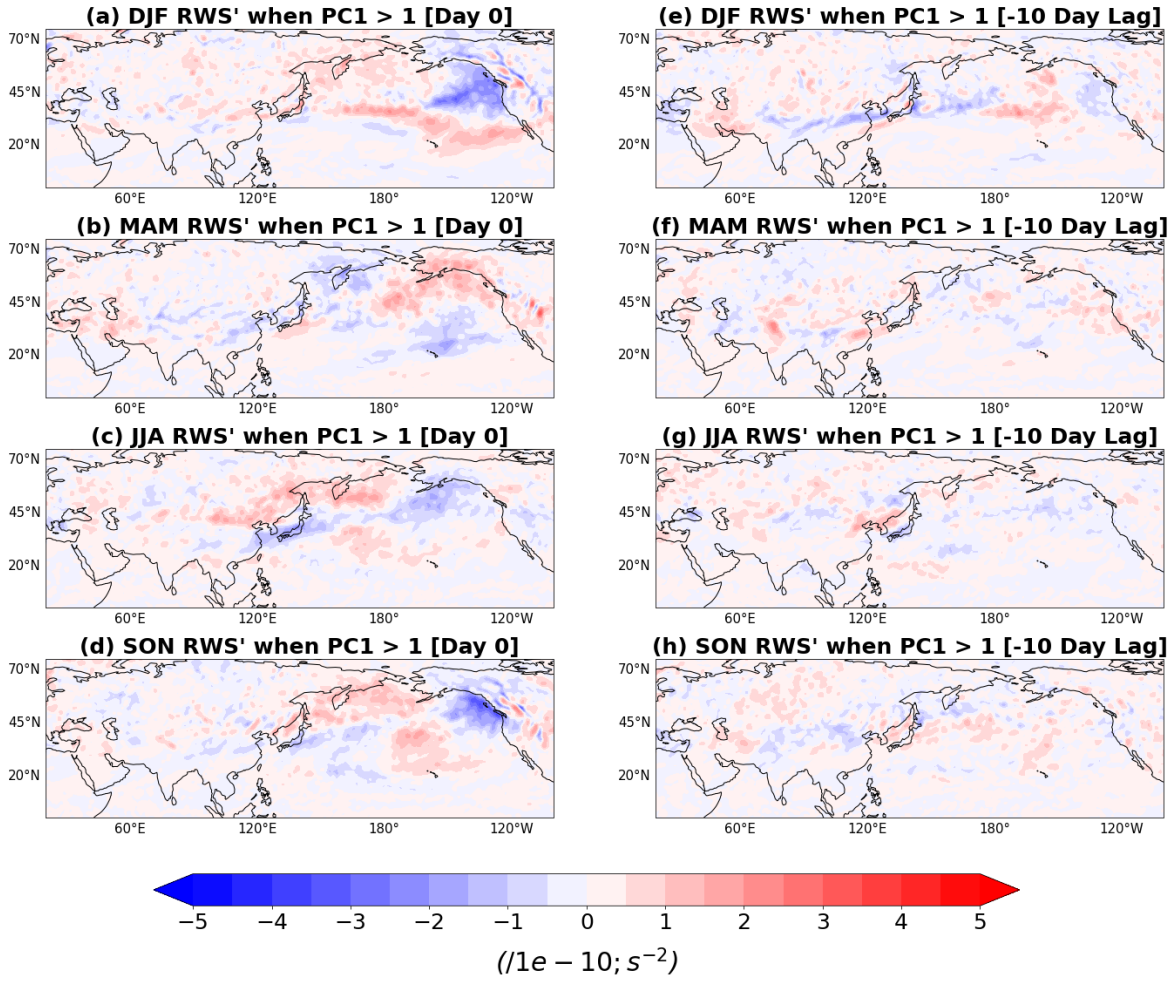

Figure 3.3: Subplotted seasonal composite of the MJO-generated RWS' for a positive PC1 index. Day-0 indicates the day when the PC1 > 1 and Day-10 Lag indicates 10 days before the PC1 > 1 is observed. Sub-panels (a,e) are winter, (b,f) are the spring, (c,g) are the summer, and (d,h) are the fall.

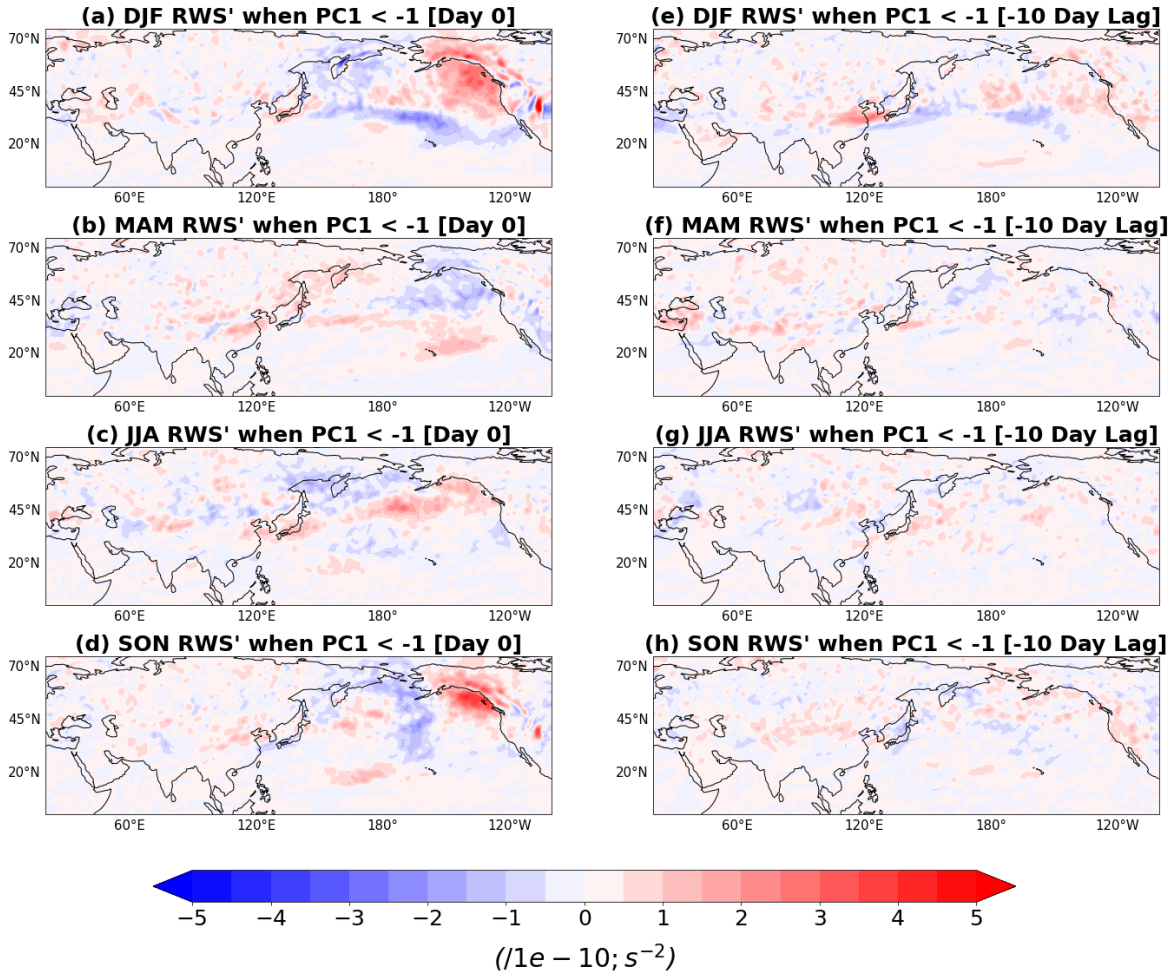

Figure 3.4: Subplotted seasonal composite of the MJO-generated RWS' for a negative PC1 index. Day-0 indicates the day when the PC1 < -1 and Day-10 Lag indicates 10 days before the PC1 < -1 is observed. Sub-panels (a,e) are winter, (b,f) are the spring, (c,g) are the summer, and (d,h) are the fall.

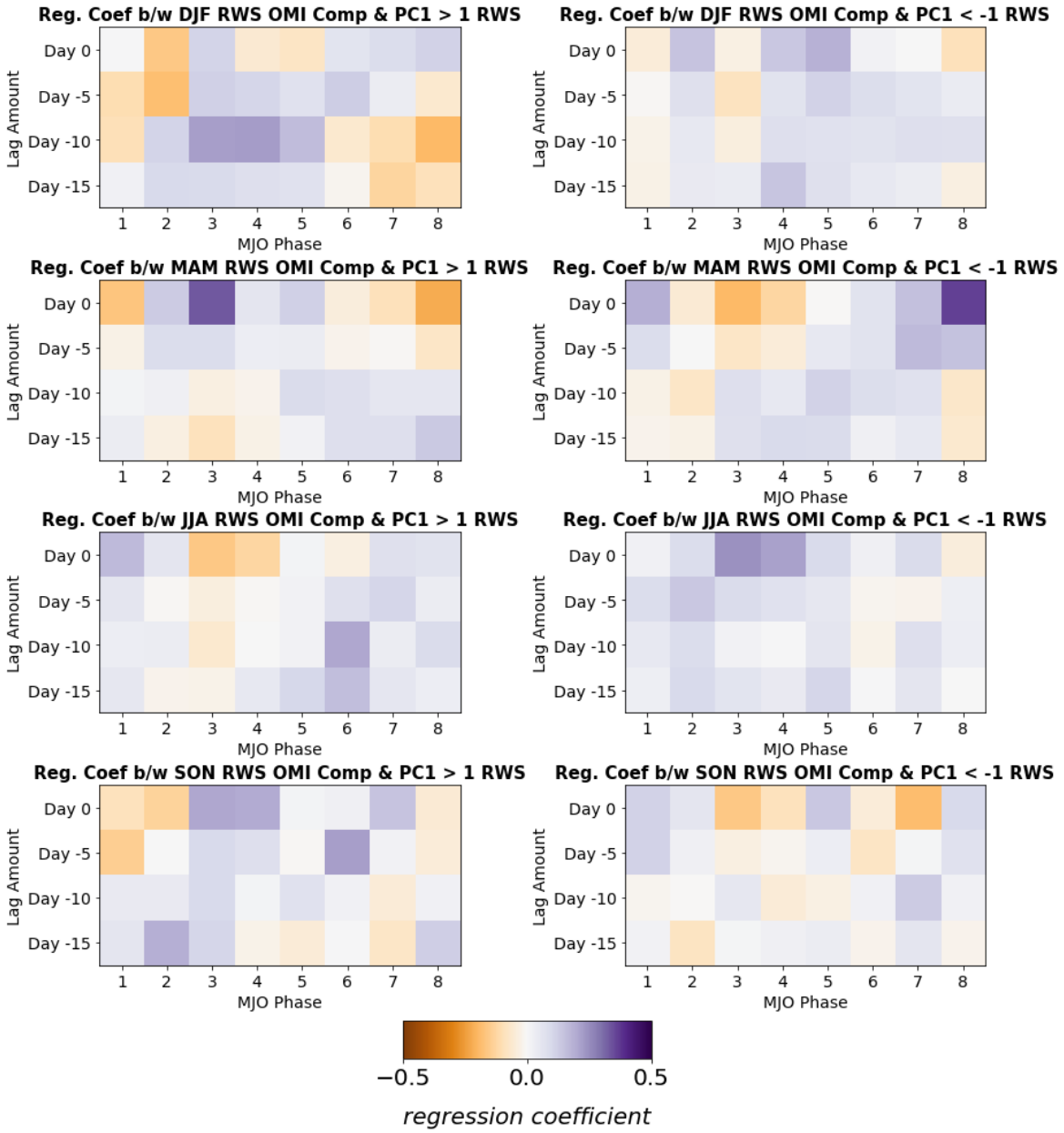

Figure 3.5: Subplottted seasonal regression coefficients between the OMI RWS' composites and the positive and negative PC1's RWS' for Day-0 and Day-5, -10, -15 lags. Sub-panels (a,e) are winter, (b,f) are the spring, (c,g) are the summer, and (d,h) are the fall.

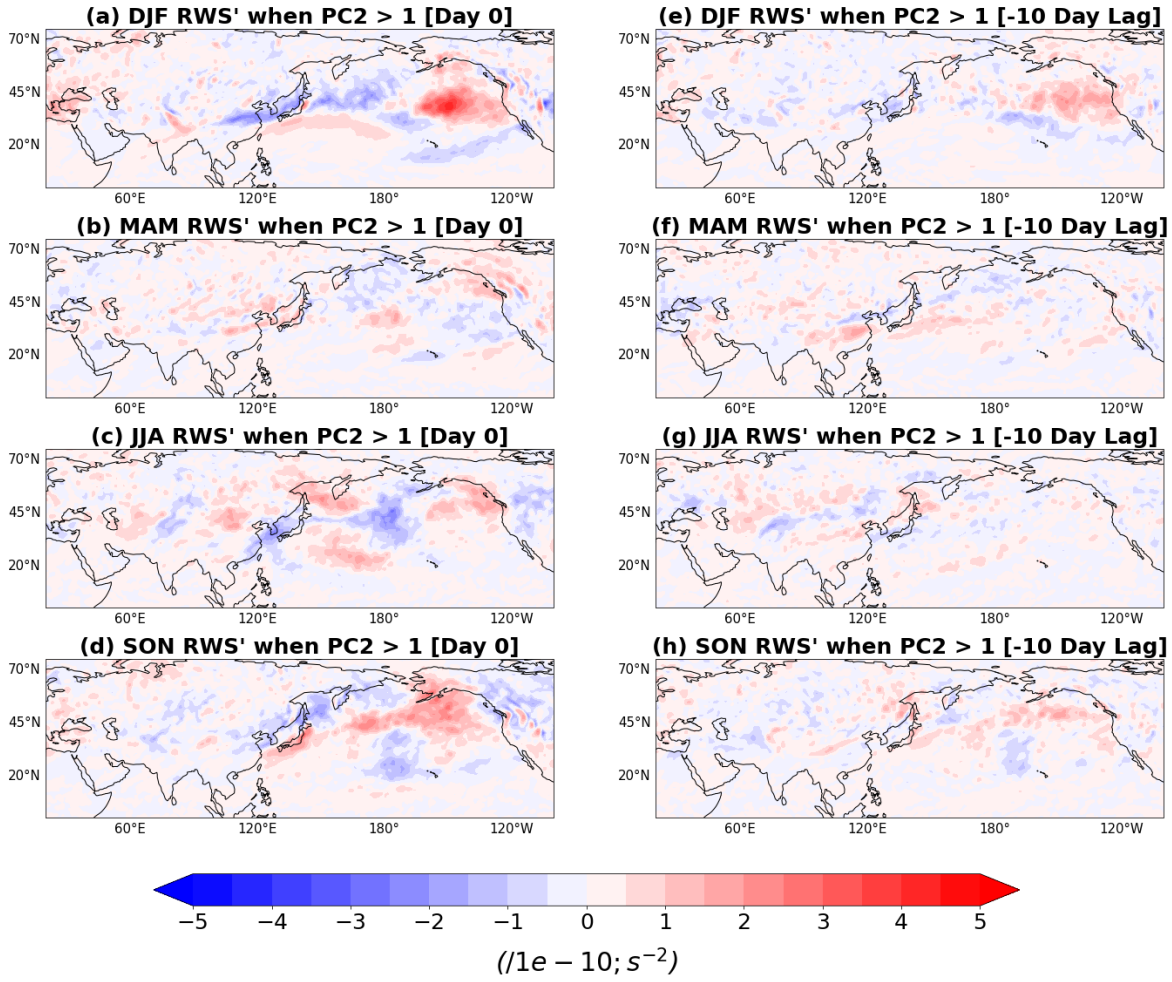

Figure 3.6: Subplotted seasonal composite of the MJO-generated RWS' for a positive PC2 index. Day-0 indicates the day when the PC2 > 1 and Day-10 Lag indicates 10 days before the PC2 > 1 is observed. Sub-panels (a,e) are winter, (b,f) are the spring, (c,g) are the summer, and (d,h) are the fall.

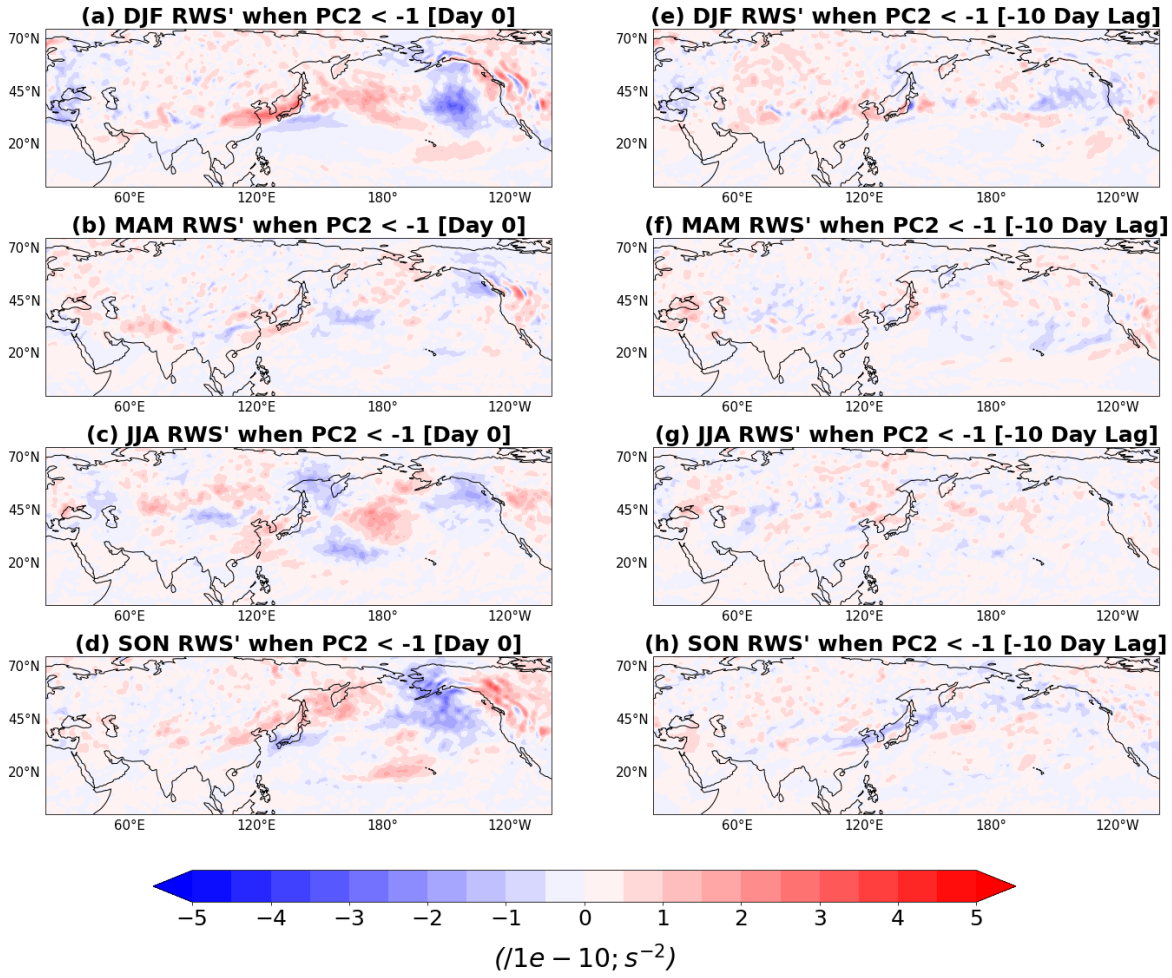

Figure 3.7: Subplotted seasonal composite of the MJO-generated RWS' for a negative PC2 index. Day-0 indicates the day when the PC2 < -1 and Day-10 Lag indicates 10 days before the PC2 < -1 is observed. Sub-panels (a,e) are winter, (b,f) are the spring, (c,g) are the summer, and (d,h) are the fall.

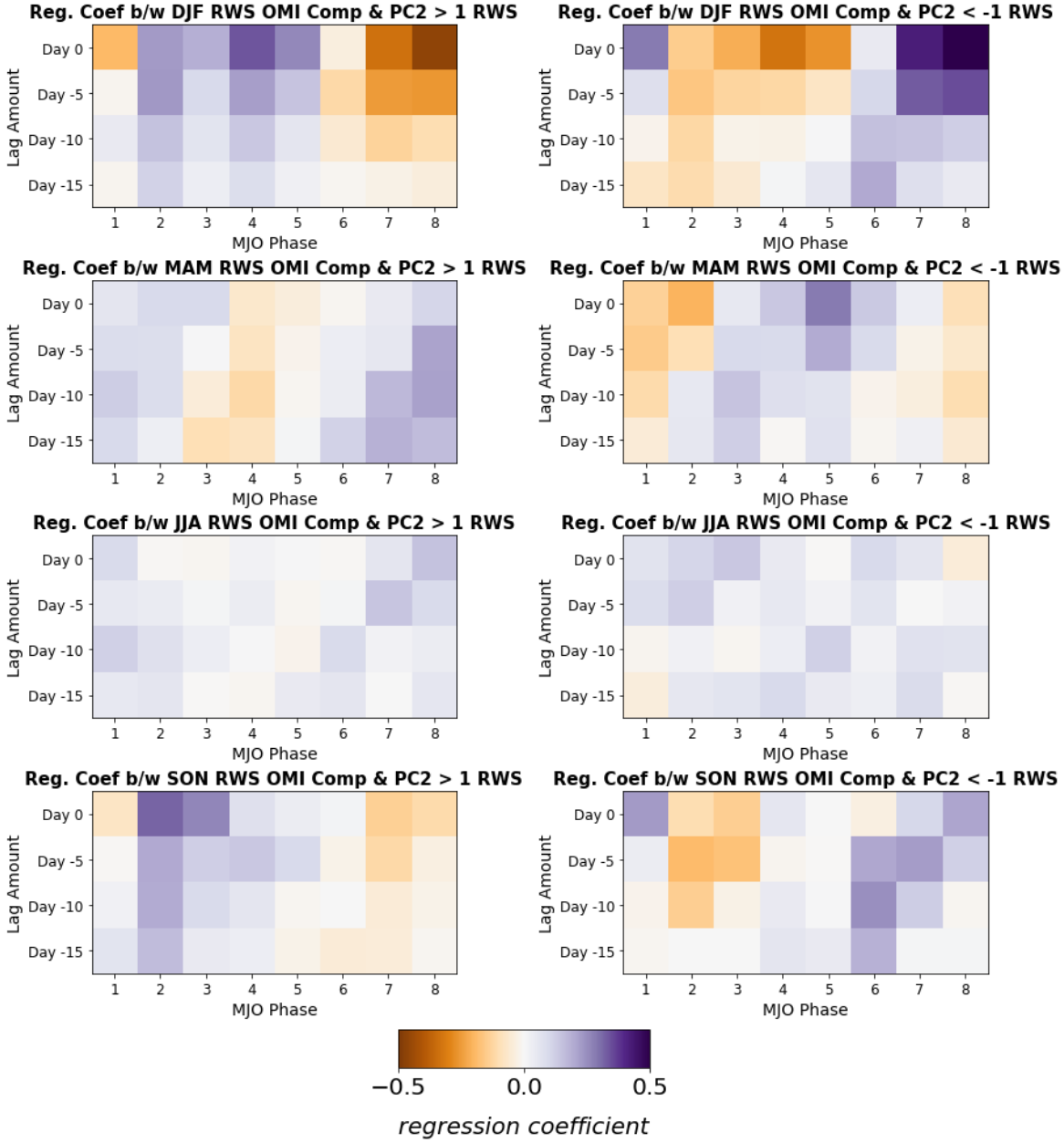

Figure 3.8: Subplottted seasonal regression coefficients between the OMI RWS' composites and the positive and negative PC2's RWS' for Day-0 and Day-5, -10, -15 lags. Sub-panels (a,e) are winter, (b,f) are the spring, (c,g) are the summer, and (d,h) are the fall.

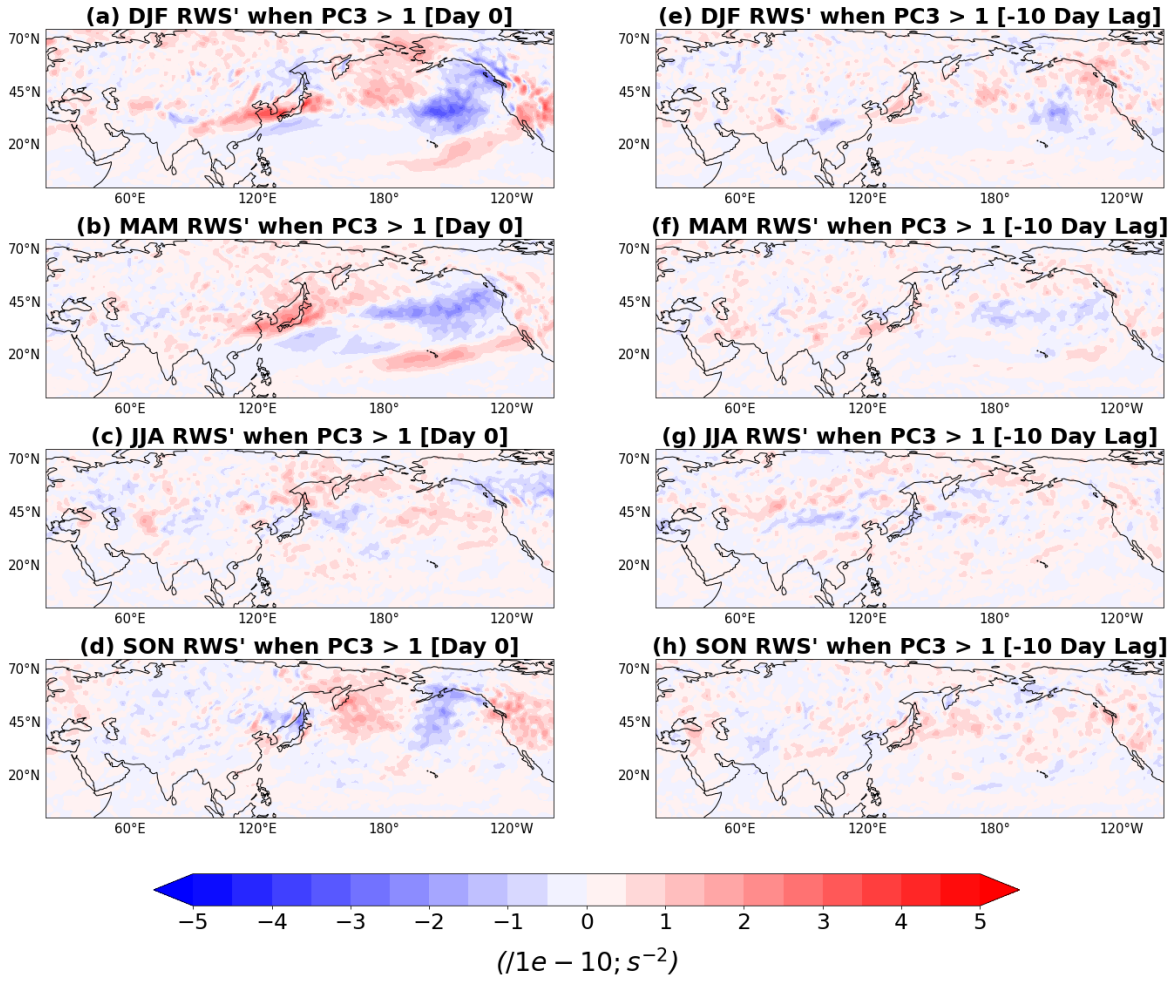

Figure 3.9: Subplotted seasonal composite of the MJO-generated RWS' for a positive PC3 index. Day-0 indicates the day when the PC3 > 1 and Day-10 Lag indicates 10 days before the PC3 > 1 is observed. Sub-panels (a,e) are winter, (b,f) are the spring, (c,g) are the summer, and (d,h) are the fall.

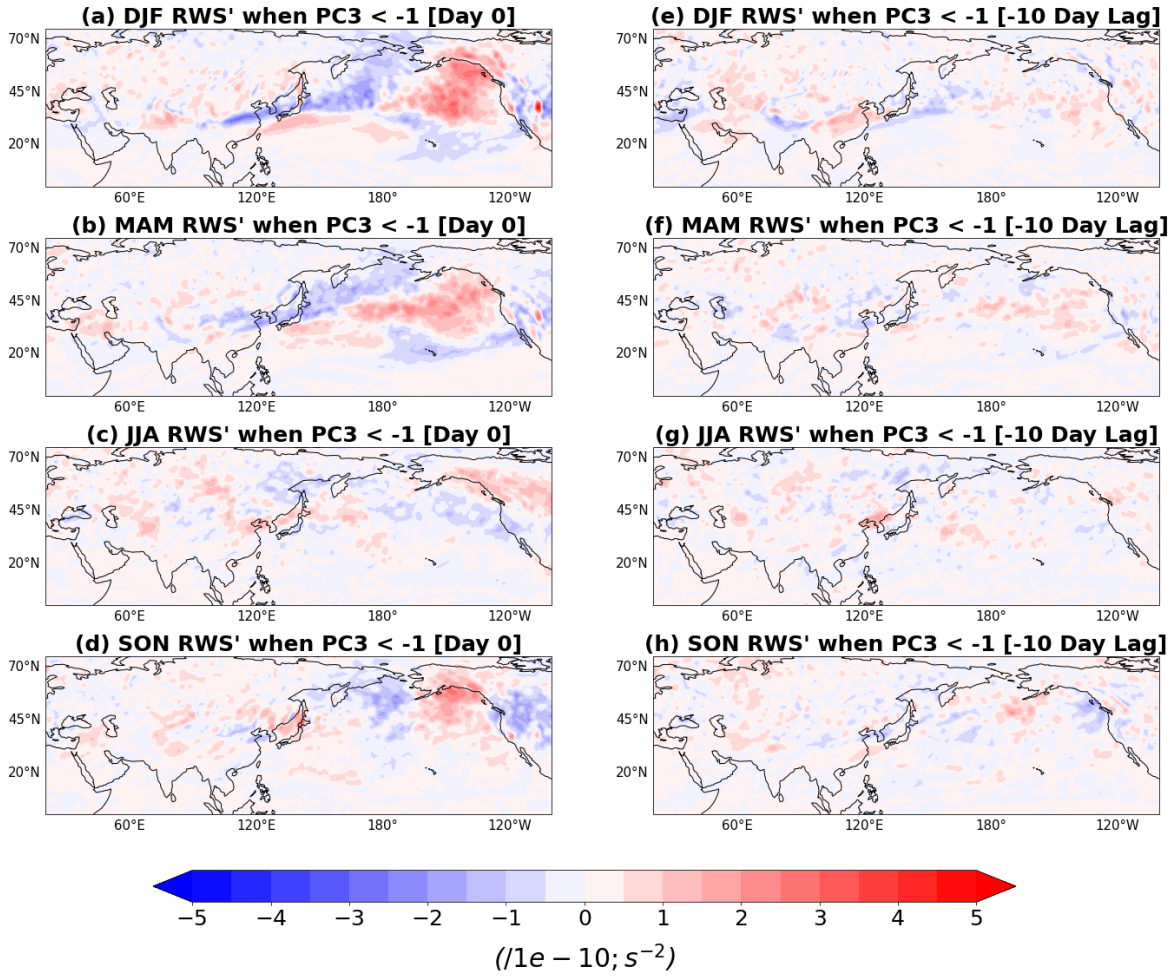

Figure 3.10: Subplotted seasonal composite of the MJO-generated RWS' for a negative PC3 index. Day-0 indicates the day when the PC3 < -1 and Day-10 Lag indicates 10 days before the PC3 < -1 is observed. Sub-panels (a,e) are winter, (b,f) are the spring, (c,g) are the summer, and (d,h) are the fall.

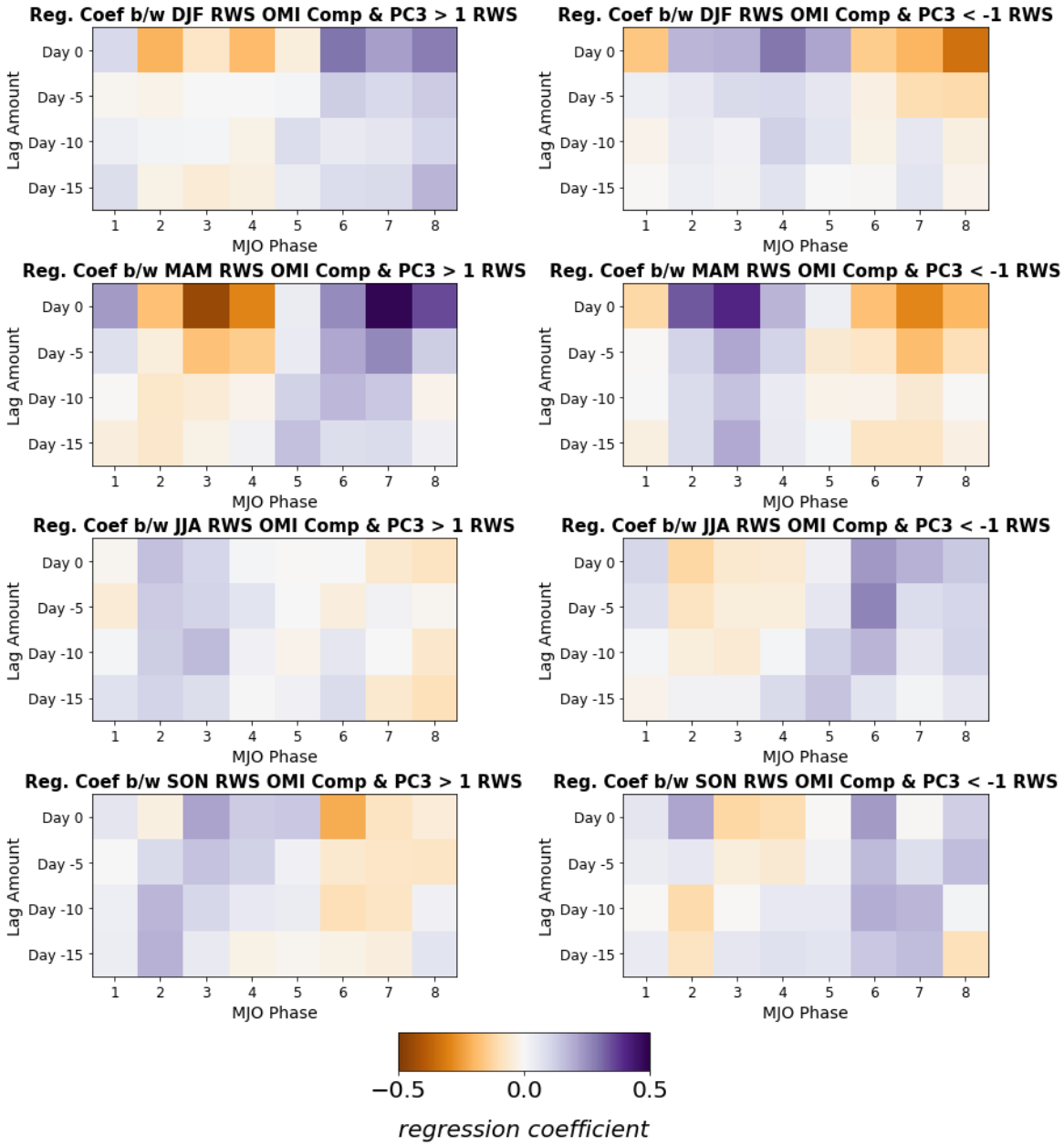

Figure 3.11: Subplottted seasonal regression coefficients between the OMI RWS' composites and the positive and negative PC3's RWS' for Day-0 and Day-5, -10, -15 lags. Sub-panels (a,e) are winter, (b,f) are the spring, (c,g) are the summer, and (d,h) are the fall.

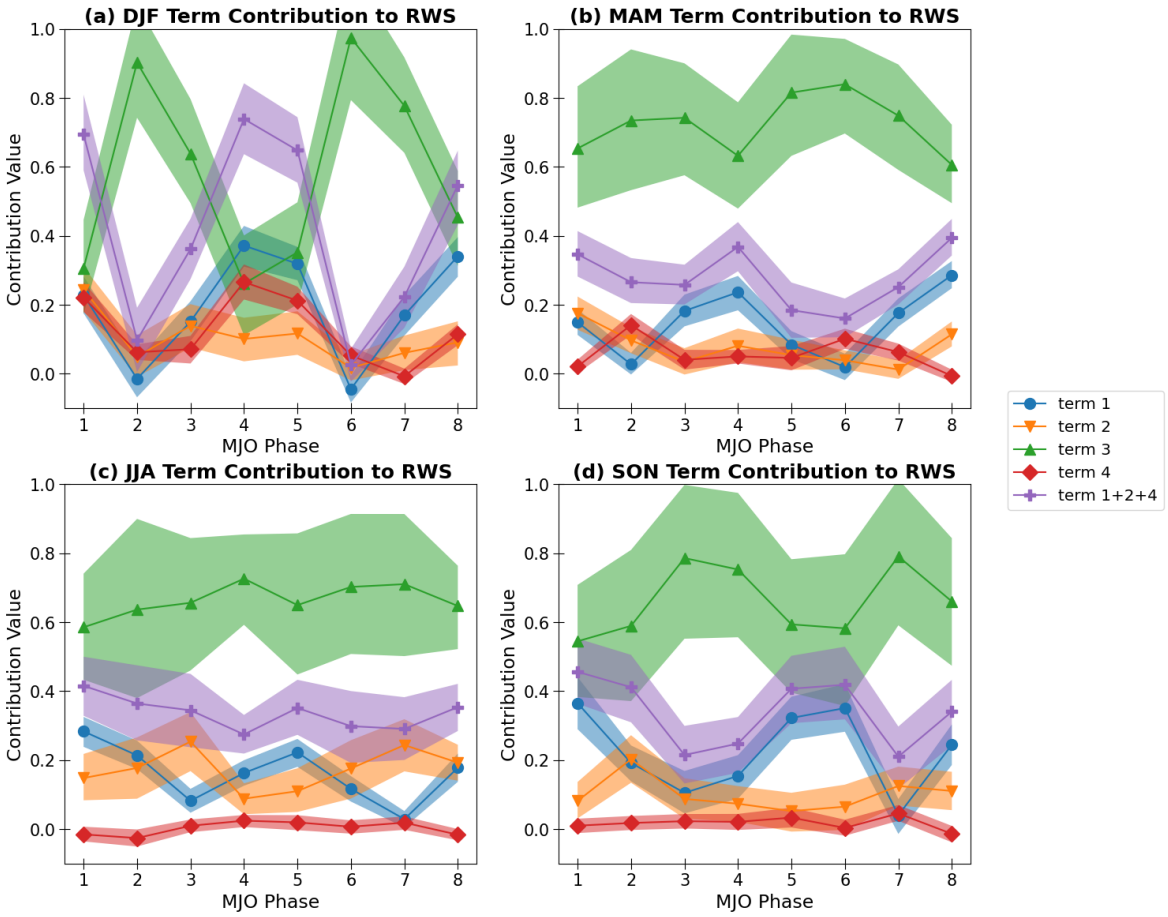

Figure 3.12: Subplotted seasonal term contribution to the anomalous RWS using Eqn. 3.2 . Sub-panels are (a) winter, (b) spring, (c) summer, and (d) fall. Error bars are the bottom and top 5% of a Monte Carlo simulation of 1000 iterations.

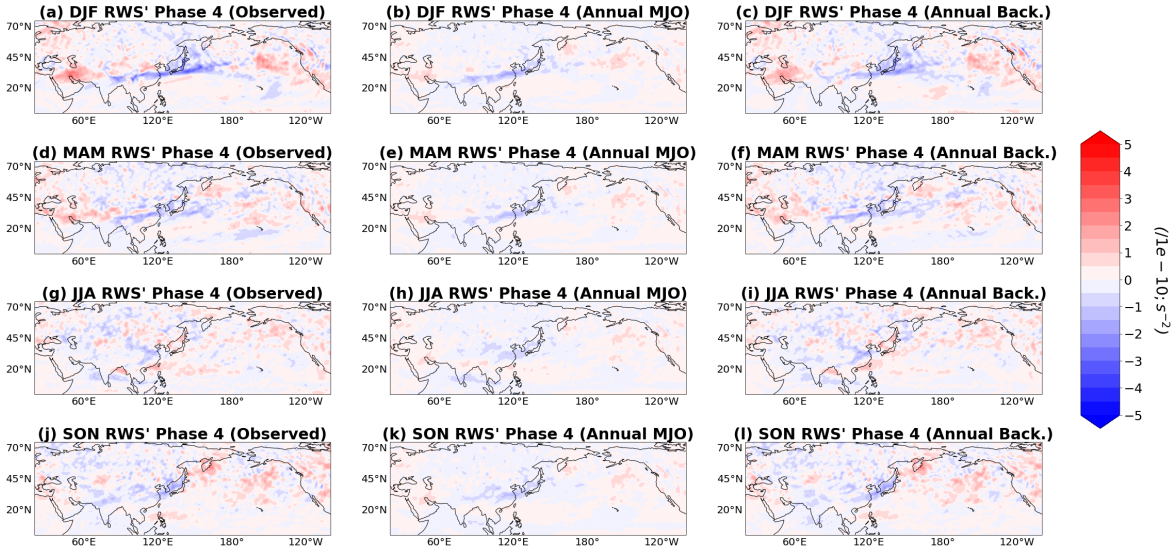

Figure 3.13: Subplotted seasonal phase 4 composite of the observed RWS', the Annual MJO RWS' from Eqn. 3.3. and the Annual Background RWS' from Eqn. 3.4. Subpanels are (a,b,c) are winter, (d,e,f) are spring, (g,h,i) are summer, and (j,k,l) are fall.

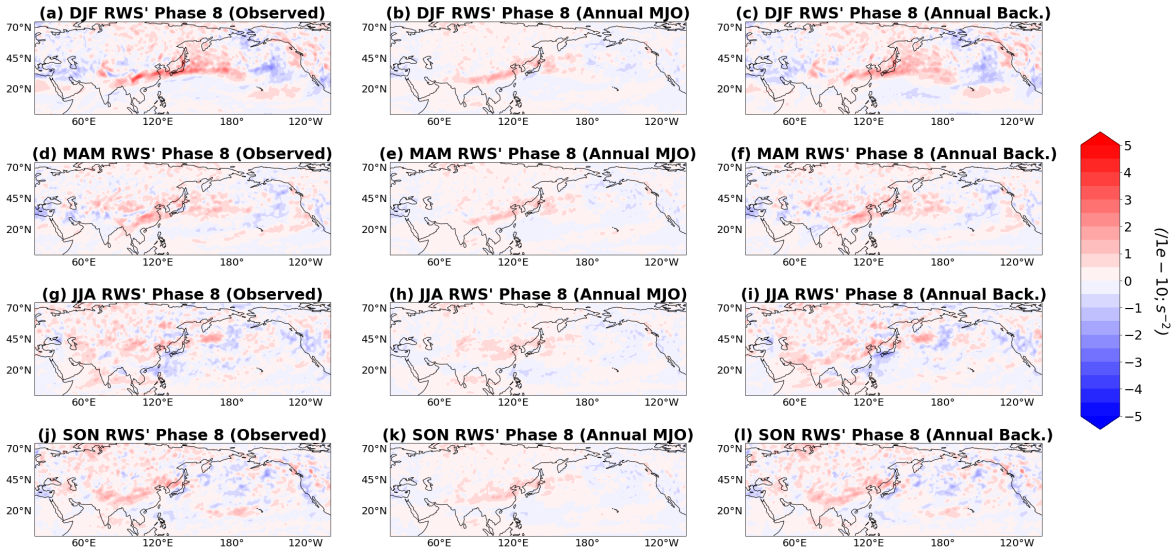

Figure 3.14: Subplotted seasonal phase 8 composite of the observed RWS', the Annual MJO RWS' from Eqn. 3.3. and the Annual Background RWS' from Eqn. 3.4. Subpanels are (a,b,c) are winter, (d,e,f) are spring, (g,h,i) are summer, and (j,k,l) are fall.

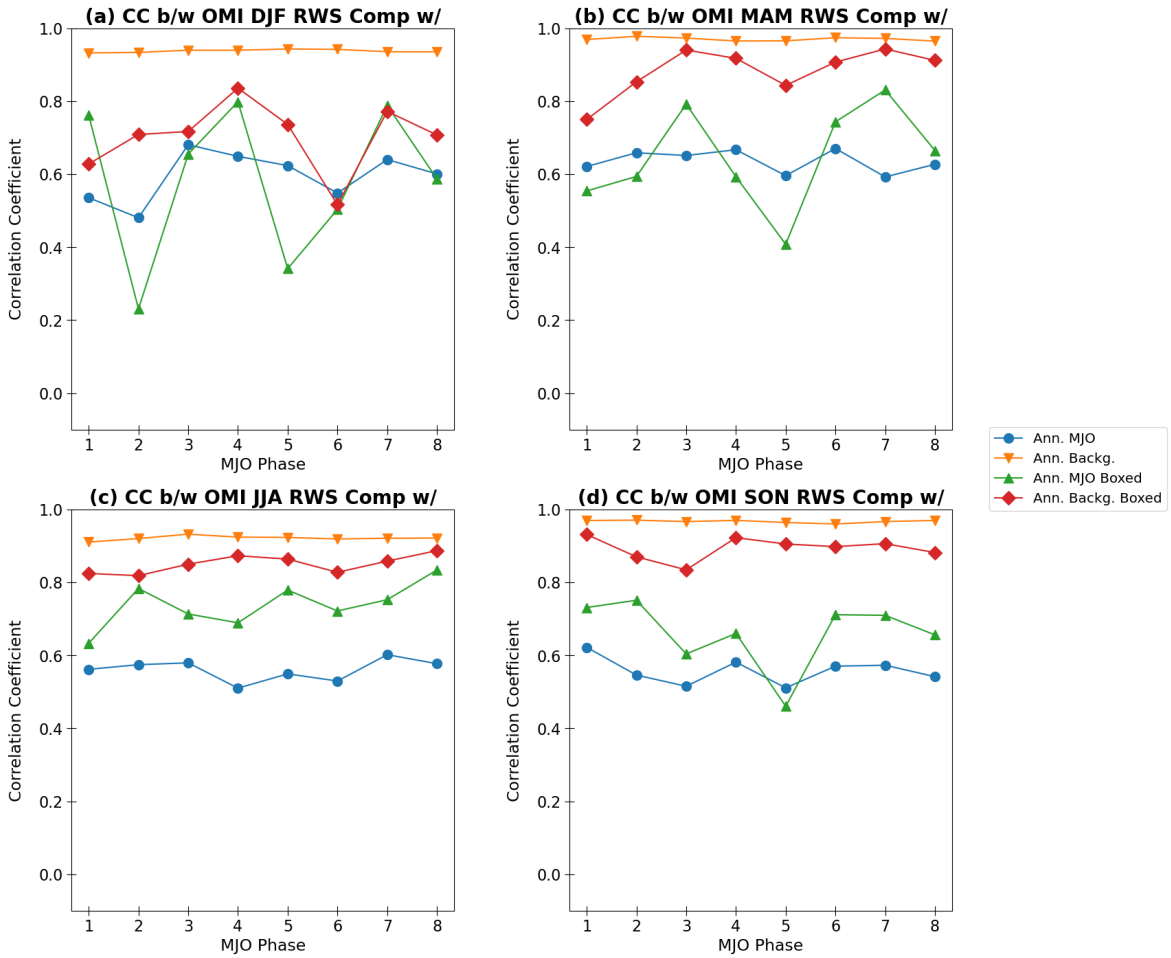

Figure 3.15: Subplotted seasonal correlation coefficients between the observed RWS' with the Annual MJO RWS' and Annual Background RWS'. Correlation coefficients were calculated for the whole domain along with a sub-domain (20-45 °N and 90-120 °E). Sub-panel (a) is winter, (b) is spring, (c) is summer, and (d) is fall.

Chapter 4

Conclusions

The objective of this work was to understand the seasonality of MJO teleconnections and what causes this seasonality. The MJO is viewed as a source of predictability on the S2S timescale and has the ability to help advance S2S forecast skill. However, studies on the MJO and its teleconnections were mainly limited to boreal winter and there lacked knowledge about the relationship in other seasons. With a better understanding of the seasonality of MJO teleconnections, we have the ability to interpret the usability of the MJO as an S2S predictor.

We first examined how the MJO teleconnections change seasonally. We demonstrated that MJO teleconnections have strong seasonality, shown by seasonally varying amplitude and location of height anomalies associated with the MJO. Our results extends on Toms et al. (2020)'s work which showed that intraseasonal variability from the MJO, during the summer, was confined to the tropics and explained less variability in the extratropics. However, the research presented here takes a step further and demonstrates what (dominant) modes in the extratropics the MJO relates to. Given that the dominant extratropical modes of circulation are different in each season, we examined if the MJO simply modulates the most dominant mode seasonally. The leading modes of the extratropics are diagnosed through EOF analysis in each season. We found that the MJO most strongly modulates the occurrence of the second leading EOF in the winter, which corresponds to the PNA. However, in other seasons, the MJO does not

strongly modulate the leading modes of the extratropics. These findings demonstrate that the knowledge of MJO teleconnections in one season is not applicable to another.

To understand why MJO teleconnections have strong seasonal variability, we examined the seasonality of MJO-generated RWS anomalies (RWS') and their relationships with the formation of leading EOFs. We found that the amplitude and location of MJO-generated RWS' vary greatly by season, which explains how the MJO strongly modulates the extratropical EOF modes in each season. The strong MJO teleconnection during winter is driven by the strongest RWS' in that season. The pattern of the RWS' in winter also matches the RWS' seen prior to the formation of the PNA (second leading EOF)(MORI and WATANABE 2008). In other seasons, the amplitude of the MJO-generated RWS' are weaker, leading to weaker MJO teleconnections. However, when the pattern of MJO-generated RWS' in other seasons matches the RWS' associated with the formation of an extratropical mode, the MJO tends to have a stronger connection to that mode. The development of RWS' pattern can occur 10 days prior to the formation of an EOF pattern, which supports that the MJO can be a useful S2S predictor for winter extratropics.

This work also revealed important processes that lead to the seasonally-dependent formation of RWS' associated with the MJO. There is disagreement between previous studies (Tseng et al. 2019; Song and Wu 2020) on which dynamical processes are the most important to the MJO-generated RWS. Furthermore, most studies look at boreal winter and it is unknown whether the same findings would be applicable in other seasons. While all the processes that generate the RWS' seasonally have some impact, the stretching of climatological absolute vorticity by the anomalous divergence from the MJO was seen to be the key process of RWS' generation. This was quantified with a seasonal term contribution to the RWS'. While previous studies like Henderson et al. (2017) assumed that the background state would drive the RWS' spatial pattern,

we showed that it is the seasonal MJO state that impacts the RWS' pattern the most. During winter, the existence of the strong subtropical jet is often thought to contribute to the formation of the RWS'. However, this work showed that the strong amplitude of the MJO during winter and its associated upper-level divergent winds contributes more dominantly to form the observed RWS' pattern. This indicates that to improve the prediction of MJO-generated teleconnections in all seasons, it is most important to accurately capture the seasonal characteristics of the MJO.

These results demonstrate that boreal winter knowledge about MJO teleconnections would have limitations if applied to other seasons. The relationships between the MJO and leading extratropical modes are weaker in other seasons, therefore, it suggests that the usability of the MJO as an S2S predictor is also limited. In winter, the presence of the MJO might be enough to trigger a teleconnection pattern. However, in other seasons, additional conditions in the tropical and extratropical regions like ENSO and variability in the North Pacific Jet may need to be in place to support MJO teleconnection generation. The current work demonstrates that the usability of the MJO as an S2S prediction tool in other seasons may depend on finding "windows of opportunities" that strengthen the ability of the MJO to form teleconnection patterns, such as inter-annual variabilities (QBO and ENSO) or some constructive interference of the MJO with other convectively-coupled equatorial waves that are suggested to modulate MJO-related teleconnections (Toms et al. 2020; Arcodia et al. 2020; Gloeckler and Roundy 2013).

The approaches developed in this work can be extended to further our understanding of MJO teleconnections and their seasonality. There are many pathways that can be taken to deepen our understanding. This analysis could be conducted in regions like the Atlantic or the Southern Hemisphere, a region whose teleconnection research is limited. Due to previous knowledge that ENSO can influence MJO propagation speed

and strength (Jiang et al. 2020), this, in turn, can impact MJO teleconnections. Variations in the strength, duration, and positioning of MJO teleconnection patterns with ENSO were seen in boreal winter (Roundy et al. 2010), and it would be interesting to break down our results of MJO teleconnection events to years of El Niño, La Niña, and neutral conditions to see the differences seasonally. Due to the importance of the NPJ generating the RWS' within its region, there was a study that separated the joint North Pacific-North Atlantic Jet into 4 favored regimes (Winters and Attard 2022). Since NPJ's absolute vorticity plays a role in generating the RWS', it would be useful to test whether certain regimes were tied to the production of certain teleconnection patterns and/or certain seasons. Such analyses would lead to a better understanding of other factors that influence MJO teleconnections pattern seasonally. It is worth noting a caveat of this study could be tied to the lack of independence between the MJO days. Since the MJO can be in the same phase for consecutive days, the same pattern could be presenting and overestimate the significance of these patterns. A way to fix this would be to group days together and consider them to be a single sample day/group. While the presented work demonstrates the seasonality of MJO teleconnections via the generation of the RWS', there are limitations due to its linearity and evaluation at only one level. With this, more work needs to be done to better quantify the role of the background state and nonlinear processes to the generation of teleconnections.

Altogether, this work illustrates the seasonality of the MJO teleconnections and explains why these teleconnections varied in each season through the generated RWS'. Furthermore, the work highlights the importance of accurate simulations of the MJO seasonally to improve both the prediction skill of the MJO teleconnections and the usability of the MJO as an S2S predictor.

Reference List

Adames, Á. F., J. M. Wallace, and J. M. Monteiro, 2016: Seasonality of the structure and propagation characteristics of the mjo. *Journal of the Atmospheric Sciences*, **73 (9)**, 3511 – 3526, https://doi.org/10.1175/JAS-D-15-0232.1, URL https://journals.ametsoc.org/view/journals/atsc/73/9/jas-d-15-0232.1.xml.

Arcodia, M. C., B. P. Kirtman, and L. S. P. Siqueira, 2020: How mjo teleconnections and enso interference impacts u.s. precipitation. *Journal of Climate*, **33 (11)**, 4621 – 4640, https://doi.org/https://doi.org/10.1175/JCLI-D-19-0448.1, URL https://journals.ametsoc.org/view/journals/clim/33/11/jcli-d-19-0448.1.xml.

Belanger, J. I., J. A. Curry, and P. J. Webster, 2010: Predictability of north atlantic tropical cyclone activity on intraseasonal time scales. *Monthly Weather Review*, **138 (12)**, 4362 – 4374, https://doi.org/https://doi.org/10.1175/2010MWR3460.1, URL https://journals.ametsoc.org/view/journals/mwre/138/12/2010mwr3460.1.xml.

Cassou, C., 2008: Intraseasonal interaction between the madden–julian oscillation and the north atlantic oscillation. *Nature*, **455 (7212)**, 523–527, https://doi.org/10.1038/nature07286, URL https://doi.org/10.1038/nature07286.

Gloeckler, L. C., and P. E. Roundy, 2013: Modulation of the extratropical circulation by combined activity of the madden–julian oscillation and equatorial rossby waves during boreal winter. *Monthly Weather Review*, **141 (4)**, 1347 – 1357, https://doi.org/https://doi.org/10.1175/MWR-D-12-00179.1, URL https://journals.ametsoc.org/view/journals/mwre/141/4/mwr-d-12-00179.1.xml.

Gottschalck, J., 2014: What is the mjo, and why do we care? URL https://www.climate.gov/news-features/blogs/enso/what-mjo-and-why-do-we-care.

Henderson, S. A., E. D. Maloney, and S.-W. Son, 2017: Madden–julian oscillation pacific teleconnections: The impact of the basic state and mjo representation in general circulation models. *Journal of Climate*, **30 (12)**, 4567 – 4587, https://doi.org/https://doi.org/10.1175/JCLI-D-16-0789.1, URL https://journals.ametsoc.org/view/journals/clim/30/12/jcli-d-16-0789.1.xml.

Hersbach, H., and Coauthors, 2020: The era5 global reanalysis. *Quarterly Journal of the Royal Meteorological Society*, **146 (730)**, 1999–2049, https://doi.org/https://doi.org/10.1002/qj.3803, URL https://rmets.onlinelibrary.wiley.com/doi/abs/10.1002/qj.3803, https://rmets.onlinelibrary.wiley.com/doi/pdf/10.1002/qj.3803.

Jiang, X., and Coauthors, 2020: Fifty years of research on the madden-julian oscillation: Recent progress, challenges, and perspectives. *Journal of Geophysical Research:*

Atmospheres, **125 (17)**, https://doi.org/https://doi.org/10.1029/2019JD030911, URL https://agupubs.onlinelibrary.wiley.com/doi/abs/10.1029/2019JD030911.

Kiladis, G. N., J. Dias, K. H. Straub, M. C. Wheeler, S. N. Tulich, K. Kikuchi, K. M. Weickmann, and M. J. Ventrice, 2014: A comparison of olr and circulation-based indices for tracking the mjo. *Monthly Weather Review*, **142 (5)**, 1697 – 1715, https://doi.org/10.1175/MWR-D-13-00301.1, URL https://journals.ametsoc.org/view/journals/mwre/142/5/mwr-d-13-00301.1.xml.

Kiladis, G. N., K. H. Straub, and P. T. Haertel, 2005: Zonal and vertical structure of the madden–julian oscillation. *Journal of the Atmospheric Sciences*, **62 (8)**, 2790 – 2809, https://doi.org/10.1175/JAS3520.1, URL https://journals.ametsoc.org/view/journals/atsc/62/8/jas3520.1.xml.

Leathers, D. J., B. Yarnal, and M. A. Palecki, 1991: The pacific/north american teleconnection pattern and united states climate. part i: Regional temperature and precipitation associations. *Journal of Climate*, **4 (5)**, 517 – 528, https://doi.org/10.1175/1520-0442(1991)004⟨0517:TPATPA⟩2.0.CO;2, URL https://journals.ametsoc.org/view/journals/clim/4/5/1520-0442_1991_004_0517_tpatpa_2_0_co_2.xml.

Lee, Y.-Y., and R. Grotjahn, 2019: Evidence of specific mjo phase occurrence with summertime california central valley extreme hot weather. *Advances in Atmospheric Sciences*, **36 (6)**, 589–602, https://doi.org/10.1007/s00376-019-8167-1, URL https://doi.org/10.1007/s00376-019-8167-1.

Madden, R. A., and P. R. Julian, 1971: Detection of a 40–50 day oscillation in the zonal wind in the tropical pacific. *Journal of Atmospheric Sciences*, **28 (5)**, 702 – 708, https://doi.org/10.1175/1520-0469(1971)028⟨0702:DOADOI⟩2.0.CO;2, URL https://journals.ametsoc.org/view/journals/atsc/28/5/1520-0469_1971_028_0702_doadoi_2_0_co_2.xml.

Madden, R. A., and P. R. Julian, 1972: Description of global-scale circulation cells in the tropics with a 40–50 day period. *Journal of Atmospheric Sciences*, **29 (6)**, 1109 – 1123, https://doi.org/10.1175/1520-0469(1972)029⟨1109:DOGSCC⟩2.0.CO;2, URL https://journals.ametsoc.org/view/journals/atsc/29/6/1520-0469_1972_029_1109_dogscc_2_0_co_2.xml.

Maher, P., M. E. Kelleher, P. G. Sansom, and J. Methven, 2020: Is the subtropical jet shifting poleward? *Climate Dynamics*, **54 (3)**, 1741–1759, https://doi.org/10.1007/s00382-019-05084-6, URL https://doi.org/10.1007/s00382-019-05084-6.

Miller, D. E., V. A. Gensini, and B. S. Barrett, 2022: Madden-julian oscillation influences united states springtime tornado and hail frequency. *npj Climate and Atmospheric Science*, **5 (1)**, 37, https://doi.org/10.1038/s41612-022-00263-5, URL https://doi.org/10.1038/s41612-022-00263-5.

MORI, M., and M. WATANABE, 2008: The growth and triggering mechanisms of the pna: A mjo-pna coherence. *Journal of the Meteorological Society of Japan. Ser. II*, **86 (1)**, 213–236, https://doi.org/10.2151/jmsj.86.213.

Pohl, B., and A. J. Matthews, 2007: Observed changes in the lifetime and amplitude of the madden–julian oscillation associated with interannual enso sea surface temperature anomalies. *Journal of Climate*, **20 (11)**, 2659 – 2674, https://doi.org/https://doi.org/10.1175/JCLI4230.1, URL https://journals.ametsoc.org/view/journals/clim/20/11/jcli4230.1.xml.

Roundy, P. E., K. MacRitchie, J. Asuma, and T. Melino, 2010: Modulation of the global atmospheric circulation by combined activity in the madden–julian oscillation and the el niño–southern oscillation during boreal winter. *Journal of Climate*, **23 (15)**, 4045 – 4059, https://doi.org/https://doi.org/10.1175/2010JCLI3446.1, URL https://journals.ametsoc.org/view/journals/clim/23/15/2010jcli3446.1.xml.

Sardeshmukh, P. D., and B. J. Hoskins, 1988: The generation of global rotational flow by steady idealized tropical divergence. *Journal of Atmospheric Sciences*, **45 (7)**, 1228 – 1251, https://doi.org/https://doi.org/10.1175/1520-0469(1988)045⟨1228:TGOGRF⟩2.0.CO;2, URL https://journals.ametsoc.org/view/journals/atsc/45/7/1520-0469_1988_045_1228_tgogrf_2_0_co_2.xml.

Seo, K.-H., and H.-J. Lee, 2017: Mechanisms for a pna-like teleconnection pattern in response to the mjo. *Journal of the Atmospheric Sciences*, **74 (6)**, 1767 – 1781, https://doi.org/10.1175/JAS-D-16-0343.1, URL https://journals.ametsoc.org/view/journals/atsc/74/6/jas-d-16-0343.1.xml.

Song, L., and R. Wu, 2020: Modulation of the qbo on the mjo-related surface air temperature anomalies over eurasia during boreal winter. *Climate Dynamics*, **54 (3)**, 2419–2431, https://doi.org/10.1007/s00382-020-05122-8, URL https://doi.org/10.1007/s00382-020-05122-8.

Stan, C., D. M. Straus, J. S. Frederiksen, H. Lin, E. D. Maloney, and C. Schumacher, 2020: Review of tropical-extratropical teleconnections on intraseasonal time scales. *Reviews of Geophysics*, **55 (4)**, 902–937, https://doi.org/https://doi.org/10.1002/2016RG000538, URL https://agupubs.onlinelibrary.wiley.com/doi/abs/10.1002/2016RG000538, https://agupubs.onlinelibrary.wiley.com/doi/pdf/10.1002/2016RG000538.

Toms, B. A., E. A. Barnes, E. D. Maloney, and S. C. van den Heever, 2020: The global teleconnection signature of the madden-julian oscillation and its modulation by the quasi-biennial oscillation. *Journal of Geophysical Research: Atmospheres*, **125 (7)**, e2020JD032 653, https://doi.org/https://doi.org/10.1029/2020JD032653, URL https://agupubs.onlinelibrary.wiley.com/doi/abs/10.1029/2020JD032653, e2020JD032653 10.1029/2020JD032653, https://agupubs.onlinelibrary.wiley.com/doi/pdf/10.1029/2020JD032653.

Tseng, K.-C., E. Maloney, and E. Barnes, 2019: The consistency of mjo teleconnection patterns: An explanation using linear rossby wave theory. *Journal of Climate*, **32 (2)**, 531 – 548, https://doi.org/https://doi.org/10.1175/JCLI-D-18-0211.1, URL https://journals.ametsoc.org/view/journals/clim/32/2/jcli-d-18-0211.1.xml.

Vitart, F., and A. W. Robertson, 2018: "the sub-seasonal to seasonal prediction project (s2s) and the prediction of extreme events.". *Clim Atmos Sci*, **1 (3)**.

Wallace, J. M., and D. S. Gutzler, 1981: Teleconnections in the geopotential height field during the northern hemisphere winter. *Monthly Weather Review*, **109 (4)**, 784 – 812, https://doi.org/https://doi.org/10.1175/1520-0493(1981)109⟨0784:TITGHF⟩2.0.CO;2, URL https://journals.ametsoc.org/view/journals/mwre/109/4/1520-0493_1981_109_0784_titghf_2_0_co_2.xml.

Wang, J., H. Kim, D. Kim, S. A. Henderson, C. Stan, and E. D. Maloney, 2020: Mjo teleconnections over the pna region in climate models. part i: Performance- and process-based skill metrics. *Journal of Climate*, **33 (3)**, 1051 – 1067, https://doi.org/10.1175/JCLI-D-19-0253.1, URL https://journals.ametsoc.org/view/journals/clim/33/3/jcli-d-19-0253.1.xml.

Wheeler, M. C., and H. H. Hendon, 2004: An all-season real-time multivariate mjo index: Development of an index for monitoring and prediction. *Monthly Weather Review*, **132 (8)**, 1917 – 1932, https://doi.org/10.1175/1520-0493(2004)132⟨1917:AARMMI⟩2.0.CO;2, URL https://journals.ametsoc.org/view/journals/mwre/132/8/1520-0493_2004_132_1917_aarmmi_2.0.co_2.xml.

Winters, A. C., and H. E. Attard, 2022: North pacific and north atlantic jet covariability and its relationship to cool season temperature and precipitation extremes. *Weather and Forecasting*, **37 (9)**, 1581 – 1600, https://doi.org/https://doi.org/10.1175/WAF-D-21-0203.1, URL https://journals.ametsoc.org/view/journals/wefo/37/9/WAF-D-21-0203.1.xml.

Zhang, C., and M. Dong, 2004: Seasonality in the madden–julian oscillation. *Journal of Climate*, **17 (16)**, 3169 – 3180, https://doi.org/10.1175/1520-0442(2004)017⟨3169:SITMO⟩2.0.CO;2, URL https://journals.ametsoc.org/view/journals/clim/17/16/1520-0442_2004_017_3169_sitmo_2.0.co_2.xml.